CATO Workpackage WP 4.1

Deliverable WP 4.1-3-05

Subsurface mineralisation:

Rate of CO_2 mineralisation and geomechanical effects on host and seal formations

Behaviour of the CO_2-H_2O system and preliminary mineralisation model and experiments

S.J.T.Hangx
HPT Laboratory, Department of Earth Sciences
Utrecht University

Submitted to Shell International Exploration and Production (leader CATO WP 4.1).
Work performed in the framework of Shell contract 4600002284
December 2005

Table of contents

1. Introduction

1.1 CATO and the present PhD project

There is rapidly converging agreement that CO_2 emissions need to be reduced in order to limit climate change and global warming effects. One way of disposing of carbon dioxide, which may be reasonable in the short term, is by subsurface mineralisation (Bachu et al., 1996; Holloway, 1996; Wawersik et al., 2001). This entails the injection of CO_2 into suitable subsurface rock formations where it will be, partly, converted into carbonates, and hence rendered immobile. Subsurface mineralisation generates extra CO_2 storage potential, in addition to CO_2 storage by hydrodynamic trapping, i.e. CO_2 storage by dissolving carbon dioxide into the pore water. Research on subsurface mineralisation is the main focus of Work Package 4.1 of the Dutch national research programme CATO (CO_2 capture, transport and storage). CATO aims to build up a strong and coherent knowledge network, combined with adequate dissemination of knowledge, in the area of CO_2 capture, transport and storage. This network will gather and validate knowledge, develop novel technologies for CO_2 capture and storage, built up capacity to implement these technologies, and explore to which extent specific Clean Fossil Fuel options are acceptable to society.

The principle behind CO_2 sequestration by subsurface mineralisation is based on a number of sequential chemical reactions: (1) CO_2 dissolves in the reservoir water to form carbonic acid, and subsequently bicarbonate; (2) the bicarbonate reacts with cations present in the reservoir water in order to form stable carbonates. This whole process can be represented schematically as

$$CO_{2\,(g)} + H_2O_{(l)} \leftrightarrow H_2CO_{3\,(aq)} \leftrightarrow H^+_{(aq)} + HCO_3^-{}_{(aq)} \quad (1)$$
$$Mg^{2+}_{(aq)} + HCO_3^-{}_{(aq)} \leftrightarrow H^+_{(aq)} + MgCO_{3\,(s)} \text{ (magnesite)} \quad (2a)$$
$$Ca^{2+}_{(aq)} + HCO_3^-{}_{(aq)} \leftrightarrow H^+_{(aq)} + CaCO_{3\,(s)} \text{ (calcite)} \quad (2b)$$
$$Fe^{2+}_{(aq)} + HCO_3^-{}_{(aq)} \leftrightarrow H^+_{(aq)} + FeCO_{3\,(s)} \text{ (siderite)} \quad (2c)$$

If sufficient cations are present, these reactions can lead to the long term, safe, storage of carbon dioxide as stable carbonates. When CO_2 is injected into an impure sandstone reservoir, feldspars and clays present in the rock will act as the cation source, and protons present in the reservoir water, as a result of carbon dioxide dissolution, will leach out the necessary cations from the silicate structure. In order to model the progress, efficiency and geochemical/geomechanical effects of any such mineralisation process, data are needed on the response of appropriate reservoir rocks to CO_2 injections.

The present PhD project, on the rate of CO_2 mineralisation and geomechanical effects on host and seal formations, forms part of CATO Workpackage WP 4.1. It aims to

(1) determine the reaction rates of any relevant reactions taking place
(2) characterise the bulk uptake rate of CO_2
(3) determine the petrophysical factors that affect reaction
(4) determine the effect of reaction on the porosity, permeability and geomechanical response of the host and seal rock
(5) give implications for the choice of suitable sites or downhole additives.

Data produced will be incorporated into the Shell numerical modelling work on subsurface mineralisation within CATO WP 4.1.

1.2 Scope of this report

In our first report within the present PhD project, a careful study was made on the thermodynamic and kinetic data available in the literature for the reacting and precipitating minerals (Hangx, 2005). The present report incorporates a study on the thermodynamic properties of the water, CO_2 and the water-CO_2 system.

As the concentration of aqueous CO_2 in solution, and hence the extent of CO_2-rock interaction, are important to make an estimate of the amount of carbon dioxide that can be stored by dissolution and reaction, knowledge of the solubility of CO_2 in pure water and in salt solutions is also necessary. In past decades, there have been many experimental studies on the CO_2-H_2O and CO_2-H_2O-salt systems, over a wide pressure-temperature range, either to study the thermodynamic properties, by deriving Equations of State, of the components or to determine the solubility of carbon dioxide in aqueous

solution. This report gives an overview of the available literature on the thermodynamic properties of the CO_2-H_2O system and the solubility of CO_2 in aqueous solution, as well as recommendations on the use of this data. The model for the rate of mineralisation of a feldspathic sandstone, derived earlier (Hangx, 2005), is revised, and a new model is presented, which also predicts constraints on the porosity-permeability evolution of a sandstone reservoir. All symbols used are summarised in Table 1. The report will be concluded with a description of revisions to our experimental designs and preliminary results will be presented. The first experiments aim to determine the type and rate of several basic reactions occurring during CO_2 injection in a sandstone reservoir. One of those reactions is that of Ca-rich feldspar, e.g. anorthite, reacting with CO_2 to form both calcite and kaolinite

$$CaAl_2Si_2O_{8\,(s)} + CO_{2\,(g)} + 2H_2O_{(l)} \leftrightarrow CaCO_{3\,(s)} + Al_2Si_2O_5(OH)_{4\,(s)} \qquad (3)$$

Systematically performed experiments at various $P(CO_2)$, temperature, and grain size will provide reaction rate equations, which are most likely rate-limited by the dissolution of the feldspar and phyllosilicate phases, or the precipitation of clays, and not by the dissolution of carbon dioxide or the precipitation of calcite.

Table 1 Symbols list

symbol, definition [units]		*symbol, definition [units]*	
a_i	activity of species *i*	M_i	maximum amount of carbonate precipitated as a function of *i* [kg]
A_s	total surface area [m^2]	N_{grains}	number of grains
A_{grain}	surface area of a grain [m^2]	N	coordination number
d	grain size [μm]	P	pressure [bar]
φ	porosity	R	reaction rate [mol/m^2 s]
ϕ	fugacity coefficient	ρ_i	density of species *i* [g/cm^3]
k	reaction rate constant [s^{-1}]	T	absolute temperature [K]
m_i	mass of species *i* [kg]	W	vol.-% of water
m_i	molar mass of species *i* [g/mol]	X	vol.-% of anorthite
V	molar volume [dm^3/mol]	Z	compressibility factor
$\dot{M}$	amount of carbonate precipitated/unit volume/s [kg/m^3 s]	N_i^{moles}	number of moles of species *i*

2. Thermodynamic properties of CO_2 and H_2O

Of importance to our experimental study, and also to modelling geological sequestration of CO_2 in general, is to know the behaviour of the liquid and/or vapour phases present in the system. Therefore, a study has been made on the kinetic and thermodynamic properties of both carbon dioxide and water. Most thermodynamic properties (Lee & Kesler, 1975; Peng & Robinson, 1976; Kerrick & Jacobs, 1981; Bowers & Helgeson, 1983; Duan et al., 1992a, b, 1995; Span & Wagner, 1996; Wagner et al., 2000), as well as the solubility of carbon dioxide in aqueous solution (Nighswander et al., 1989; Carroll et al., 1991; King et al., 1992; Duan & Sun, 2003; Duan et al., 2005; Portier & Rochelle, 2005), can be described by using the appropriate PVT-relations, or Equations of State (App. 1). Phase relations can be derived from phase diagrams for H_2O and CO_2, as well as the CO_2-H_2O system, as shown in Fig. 1. The PT conditions for the critical point, and triple point, of both substances are given in Table 2. Beyond the critical point carbon dioxide and water become supercritical fluids, a phase that is neither liquid, nor gas.

Table 2 The critical properties of CO_2, and H_2O

component	*CO_2*	*H_2O*
T_c (°C)	30.9782 †	373.946 ‡
P_c (bar)	73.773 †	220.64 ‡
ρ_c (kg/m^3)	467.6 †	322 ‡
T_t (°C)	-56.558 †	0.01 *
P_t (bar)	5.1795 †	$6.1173 \cdot 10^{-3}$ *

† Span & Wagner (1996); ‡ Wagner et al. (2000); * Handbook of Physics and Chemistry (Lide, 2004)

In order to evaluate the solubility of CO_2 in aqueous solutions it is necessary to investigate the behaviour of the separate pure end members. Equations of State have been widely used in the study of solubility of gases in aqueous solutions and are often found at the basis of solubility models

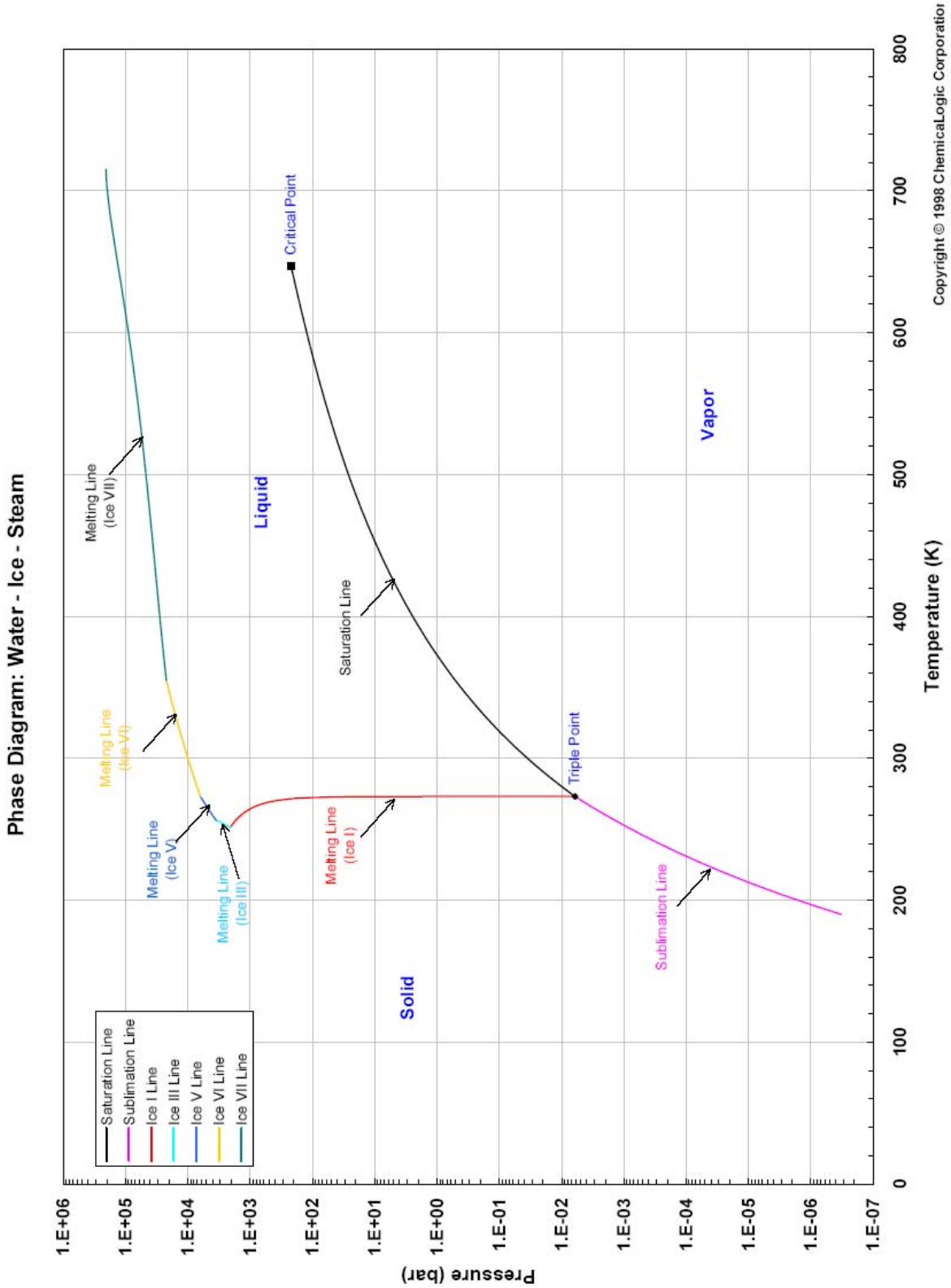

Fig. 1a Phase diagram showing the various phases of pure water at given pressures and temperatures *(Copyright © 1999 ChemicaLogic Corporation, 99 South Bedford Street, Suite 207, Burlington, MA 01803 USA. All rights reserved).*

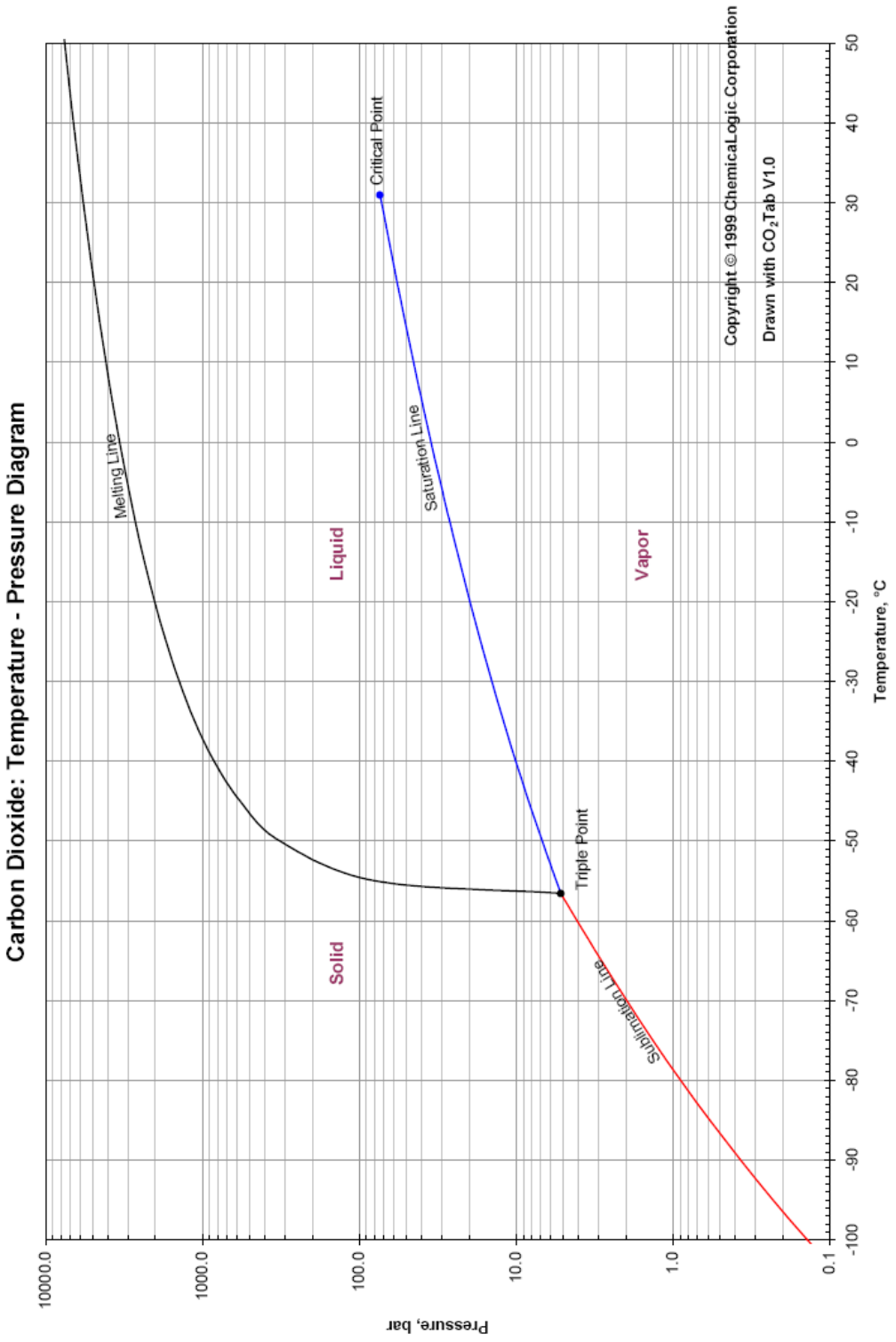

Fig. 1b Phase diagram for showing the various phases of pure CO_2 as a function of pressure and temperature *(Copyright © 1999 ChemicaLogic Corporation, 99 South Bedford Street, Suite 207, Burlington, MA 01803 USA. All rights reserved).*

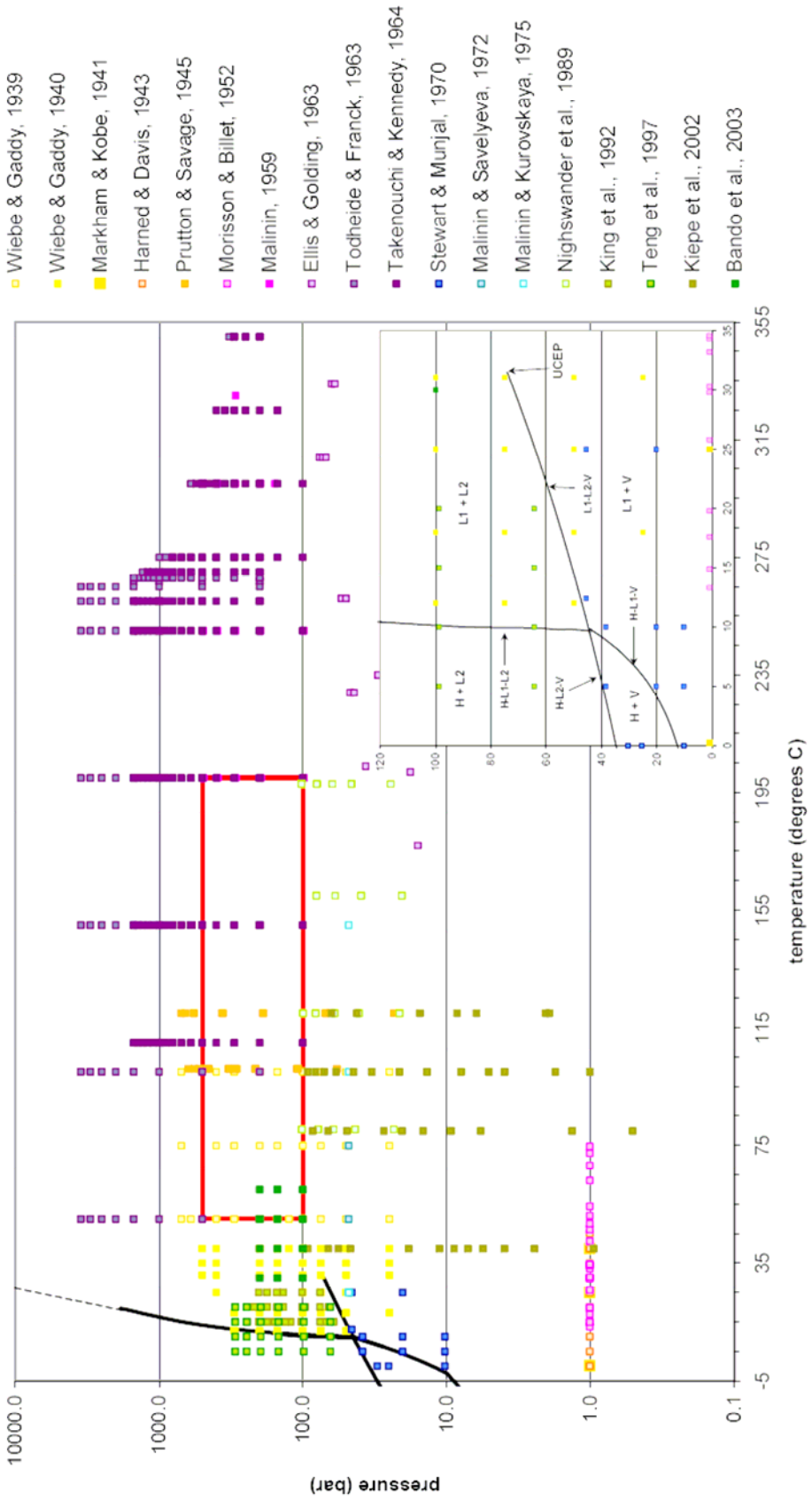

Fig. 1c Phase diagram for the CO_2-H_2O system showing the various phases as a function of temperature and pressure. The in-set shows an enlarged PT-diagram of the CO_2-H_2O system. The curves are three-phase coexistence curves: H = hydrate, L1 = water-rich liquid, L2 = CO_2-rich liquid, and V = vapor phase (Takenouchi & Kennedy, 1965a; Ng & Robinson, 1985; Wendland et al., 1999). UCEP is the upper critical point of the CO_2-H_2O system. Data points are from various experimental studies, summarized in Table 3, and show the PT-conditions at which the solubility of CO_2 in pure water has been determined. In the supercritical region, additionally, the solubility of water in CO_2 has been measured. Also indicated is the range of PT-conditions of interest (red box).

(Nighswander et al., 1989; Carroll et al., 1991; King et al., 1992; Duan & Sun, 2003; Portier & Rochelle, 2005). Over the past decades many EOS have been developed to model the thermodynamic properties of carbon dioxide, water and carbon dioxide-water ± NaCl mixtures over a wide range of temperature and pressure (Lee & Kesler, 1975; Peng & Robinson, 1976; Kerrick & Jacobs, 1981; Bowers & Helgeson, 1983; Duan et al., 1992a, b, 1995; Span & Wagner, 1996; Wagner et al., 2000). However, some Equations of State are not applicable to the range of temperature and pressure of interest, i.e. reservoir conditions. Below follows a short description of the EOS for CO_2, H_2O and CO_2-H_2O mixtures, which are suitably accurate for conditions ranging from 50 to 200°C and 100 to 500 bars.

2.1 Equation of State for carbon dioxide

Well known Equations of State for pure carbon dioxide, water and methane have been developed by Duan et al. (1992a). Their EOS for CO_2 forms the basis of the solubility model proposed by Duan and Sun (2003; 2005). The EOS developed by Duan et al. (1992a) is used to describe the chemical potential of CO_2 in the vapour phase and is based on the EOS developed by Lee and Kesler (1975). The temperature and pressure range for which this EOS applies is 0 to 1000°C and 0 to 8000 bars.

Of equal quality is the Equation of State developed by Span and Wagner (1996), which covers the fluid region from the triple point temperature up to 826.85°C and pressures up to 8000 bars. Span and Wagner (1996) developed a new EOS for the representation of the thermodynamic properties of carbon dioxide, which is an empirical representation of the fundamental equation explicit in the Helmholtz energy. The stated fundamental equation is expressed in the form of the Helmholtz energy f with the two independent variables density ρ and temperature T. The dimensionless Helmholtz energy $\varphi = f/RT$ is usually split into an ideal gas part φ° and a residual part φ^r:

$$\varphi(\delta,\tau) = \varphi^\circ(\delta,\tau) + \varphi^r(\delta,\tau) \qquad (4)$$

where $\delta = \rho/\rho_c$ is the reduced density, i.e. the density normalised to the critical density, and $\tau = T_c/T$ is the inversed reduced temperature, i.e. the inverse of temperature normalised to critical temperature. The subscript c denotes the critical values of both density and temperature. Here the Helmholtz energy is described as a function of density and temperature; however, this is just one form of a fundamental equation and, in fact, all thermodynamic properties of pure carbon dioxide can be calculated by combing derivatives of this equation (see Table 3 in Span and Wagner (1996)).

Though there is little difference in the quality of the various EOS mentioned above, that developed by Duan et al. (1992a) is recommended and used here to represent the thermodynamic properties of carbon dioxide, as it covers the largest PT-range and is also used in the description of the CO_2-H_2O system. Therefore a description of this EOS is given in Appendix 1a.

2.2 Equation of State for water

Though Duan et al. (1992a) also developed an EOS for water, we choose to recommend to use the Equation of State released by The International Association for the properties of Water and Steam (IAPWS), for the thermodynamic properties of water (the IAWPS Industrial Formulation 1997, see Wagner et al. (2000)). This is chosen due to the diminished accuracy at low temperatures of the EOS developed by Duan et al. (1992a).

The IAWPS-97 covers temperatures from 0 to 800°C up to 1000 bars and temperatures from 800 to 2000°C up to 100 bars. The range of validity of IAWPS-97 is divided into 5 regions, as can be seen in Fig. 2, each covered by a so-called basic equation. In addition to the basic equations for regions 1, 2, and 4, so-called backward equations have been developed. These backward equations are used to speed up the calculation of properties as functions of pressure p, enthalpy h, and entropy s. The equations are numerically consistent with the basic equations and, alone or together with these basic equations, make the calculation of properties such as $T(P,h)$, $h(P,s)$, and $h'(P)$ much simpler. In Appendix 1b the basic equations for all regions are stated, as well as the equation that describes the boundary between region 2 and 3.

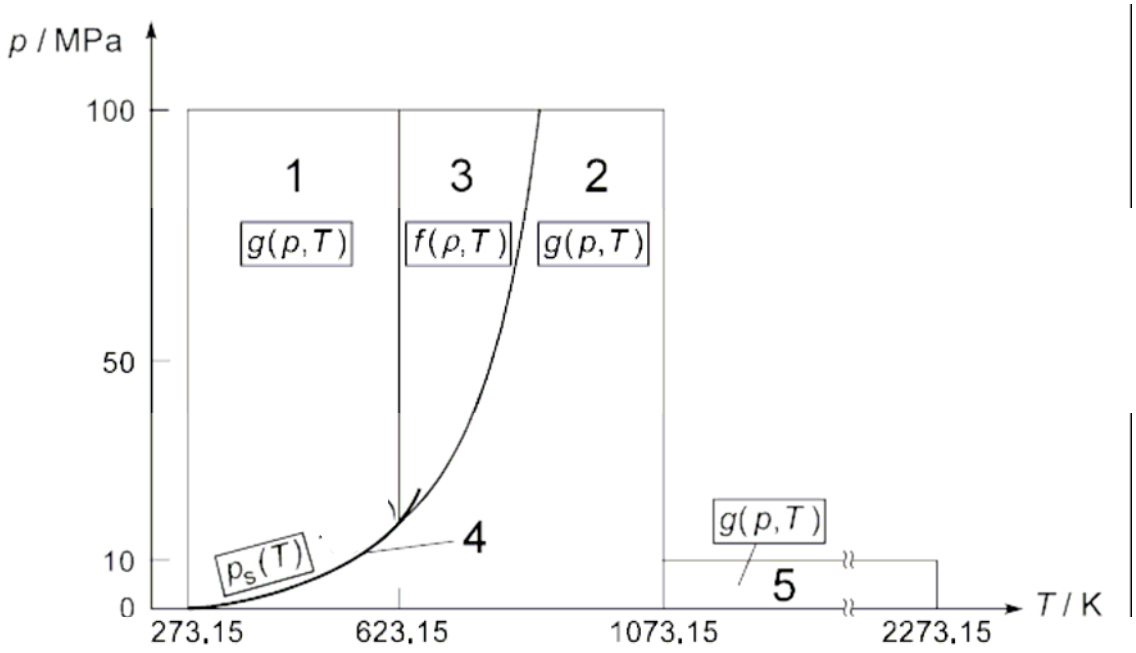

Fig. 2 Regions and equation described by IAPWS-97. All equations are shown in Appendix 1b.

2.3 CO_2-H_2O mixtures

Under reservoir conditions, water and CO_2 are two immiscible fluids, which generally means that the CO_2-rich fluid will flood on top of the water-rich fluid, due to a difference in density. However, at the contact between the two fluids, dissolution of carbon diode into the water, and also of water into the CO_2, can take place. The properties of these mixtures can be modelled using Equations of State.

Over the past decades many Equations of State have been developed to model the thermodynamic properties of the CO_2-H_2O system (Redlich & Kwong, 1949; Peng & Robinson, 1976; Kerrick & Jacobs, 1981; Duan et al., 1992b; Duan & Hu, 2004) and CO_2-H_2O-NaCl system (Bowers & Helgeson, 1983; Duan et al., 1995). Some of the EOS for the carbon dioxide-water system are not applicable to the pressure-temperature conditions of interest (Redlich & Kwong, 1949; Kerrick & Jacobs, 1981; Duan et al., 1996; Duan & Hu, 2004). The EOS developed for the calculation of the thermodynamic properties of the CO_2-water-NaCl system (Bowers & Helgeson, 1983; Duan et al., 1995) are only applicable at temperatures above 300°C, and are, hence, not described in Appendix 1c.

The Equation of State developed by Duan et al. (1992b) to describe PVTX data for the CH_4-CO_2-H_2O system is chosen here to predict the behaviour of the carbon dioxide-water system. The EOS for mixtures is an extension of their previous EOS for pure end-members, and pure system behaviour is interpolated to binary and ternary systems using mixing rules, as introduced by Duan et al. (1992b). The pressure-temperature range for applying this Equation of State is from 50 to 1000°C and 0 to 1000 bars. The EOS has the same form as their EOS for pure carbon dioxide, and is described in Appendix 1c.

The Equation of State for the carbon dioxide-water system can very well predict the effect of non-ideal mixing. The excess volume is a property that represents this behaviour in terms of a departure from the volume of an ideal mixture

$$V_{ex} = V^M - \sum x_i V_i^{pure} \qquad (5)$$

where V^M is the molar volume of the mixture and V_i^{pure} the molar volume of the separate pure species, multiplied by their molar fractions in the mixture, x_i. As can be seen in Fig. 3, the excess molar volume of the system can be quite large at lower pressures, especially at low temperature; however, at higher pressures the mixing becomes more ideal. It should be noted that the excess molar volume is calculated with increasing errors when the fraction of water in the mixture increases (Nieva & Barragán, 2003). An indication of the effect of temperature on non-ideal mixing is shown in Fig. 4, which shows the normalised fugacity of CO_2 and H_2O, as a function of the composition of the mixture, at different

temperatures. It is clear that at low temperatures mixing of the components is highly non-ideal, however, at higher temperatures mixing is close to ideal.

3. CO_2 solubility: model vs. measurement

As the concentration of aqueous CO_2 in solution is important for estimating of the amount of carbon dioxide that can be stored, and of the rate or extent of CO_2-rock interaction, knowledge of the solubility of CO_2 in pure water and salt solutions is necessary. Over the past decades there have been many experimental studies on the CO_2-H_2O and CO_2-H_2O-salt systems, over a wide pressure-temperature range (Table 3). At the same time theoretical efforts have been made to model the solubility of carbon dioxide in aqueous solutions (Nighswander et al., 1989; Carroll et al., 1991; King et al., 1992; Duan & Sun, 2003; Duan et al., 2005; Portier & Rochelle, 2005). The most complete model developed until now is that of Duan and Sun (2003; 2005), which models the solubility of CO_2 in pure water and aqueous solutions from 0 to 260°C and from 0 to 2000 bar total pressure, up to ionic strengths of 4.5 mol/kg water. The model is extended to not only predict the solubility of CO_2 in pure water and NaCl solution but also in more complex systems, which may include Ca^{2+}, K^+, Mg^{2+}, and SO_4^{2-} ions.

Below an overview is given of CO_2 solubility measurements done over the past decades, as well as the various methods that have been developed to do so. A description will be given of the Duan model, and its quality evaluated compared to experimental data.

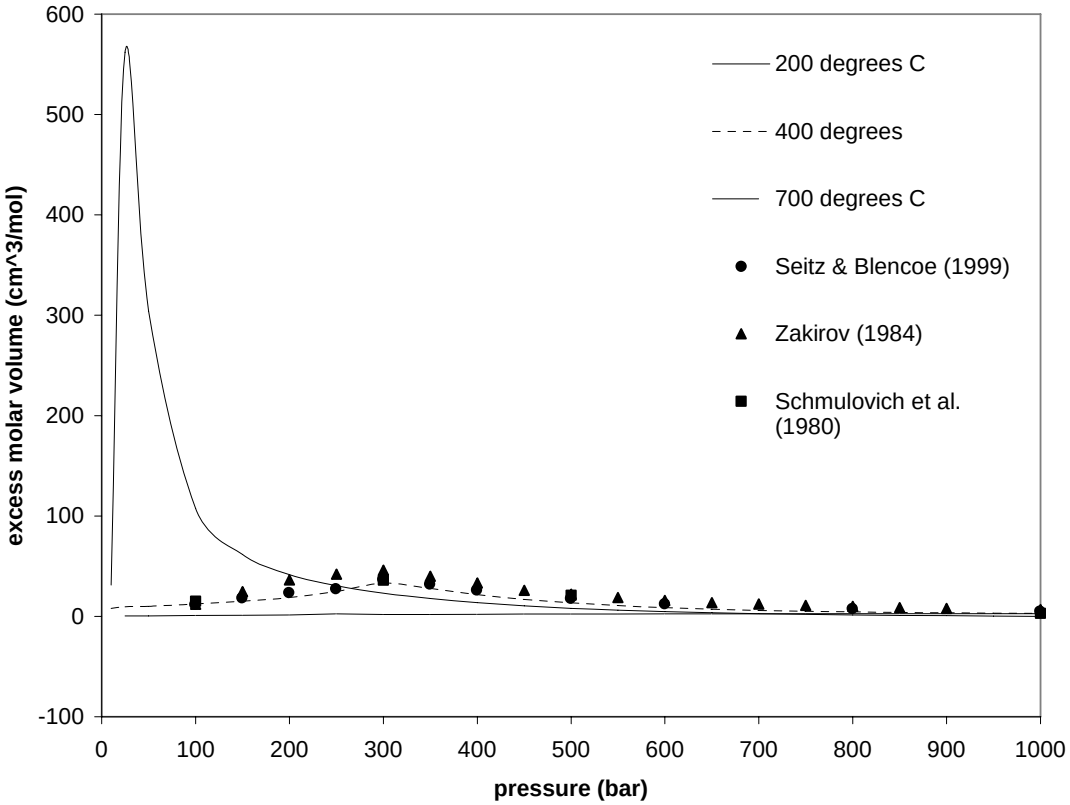

Fig. 3 Excess molar volumes for the CO_2-H_2O system at various temperatures and at $X_{CO2} = 0.6$ (Duan et al., 1992b). Data points are at 400°C (Shmulovich et al., 1980; Zakirov, 1984; Seitz & Blencoe, 1999).

3.1 Measurements done in the past

Over the past decades various methods have been used to measure the solubility of carbon dioxide in pure water and aqueous solutions. Most of the methods involve the introduction of CO_2 into a known volume solution, at the appropriate temperature and pressure, and letting it equilibrate for several hours. After equilibrium is reached a sample would be drawn from the system. Various analysing

methods can be used to measure the amount of carbon dioxide dissolved in solution. One of those is concerned with the depressurisation of the sample to atmospheric pressure and room temperature (Wiebe & Gaddy, 1939, 1940; Prutton & Savage, 1945; Tödheide & Franck, 1963; Nighswander et al., 1989). The evolved volume of carbon dioxide is measured and a correction is made for gas remaining in solution, by means of the Bunsen absorption coefficient.

Another common analyses comprises reaction of the sample with a known amount of alkaline fluid, e.g. NaOH (Takenouchi & Kennedy, 1964, 1965b; Portier & Rochelle, 2005), or $Ba(OH)_2$ (Harned & Davis, 1943; Stewart & Munjal, 1970), in excess, to neutralise the carbon dioxide. Through titration the remaining amount of OH^- can be determined and the amount of dissolved CO_2 calculated.

A third analysis is also known as the weighing method. The sample is weighed after collection and subsequently bubbled through weighed tubes, or catchers, containing CO_2-absorbing components, e.g. KOH (Malinin, 1959; Malinin & Savalyeva, 1972; Malinin & Kurovskaya, 1975) or a mixture of anhydrone, i.e. magnesium perchlorate, and Carbosorb, i.e. activated charcoal, (Ellis & Golding, 1963). Re-weighing of the tubes and the water sample than gives the mass of carbon dioxide dissolved in a certain mass of water. A disadvantage of this method with sample withdrawal is the possibility of disturbance of the sample as a result of changing PT-conditions.

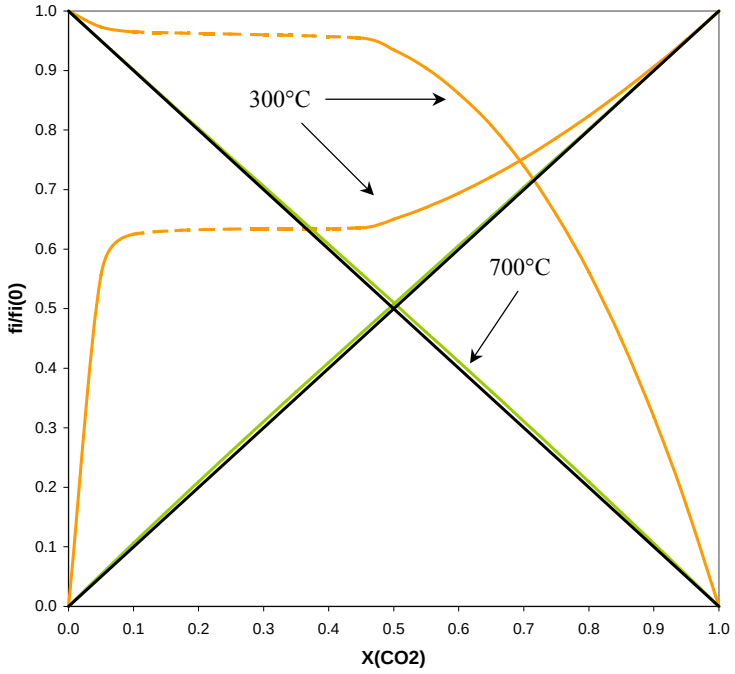

Fig. 4 The activity of CO_2 and H_2O in their mixtures and various temperatures. The dashed lines are two-phase regions and the diagonal black lines represent ideal mixing (Duan et al., 1992b).

Another well-known method for measuring the solubility of gasses in solution is the Ostwald method (Markham & Kobe, 1941; Yasunishi & Yoshida, 1979; Kiepe et al., 2002). In this case, a known volume of solution is brought into contact with a known volume of gas and left to equilibrate, at constant temperature-pressure conditions. Once equilibrium is achieved the volume of excess gas is determined and the solubility of the gas calculated.

All data points of measurements for the solubility of carbon dioxide in pure water, which are the most abundant of all solutions, are shown in the phase diagram for the carbon dioxide-water system shown in Figure 1c.

3.2 CO_2 solubility modelled

On the basis of the Equation of State developed by Duan et al. (1992a), Duan and Sun (2003; 2005) derived a theoretical model for calculating the solubility of CO_2 in pure water and aqueous NaCl solutions. They used the EOS of Duan et al. (1992a) to represent the chemical potential of carbon dioxide in the vapour phase; the interaction model of Pitzer (1973) describes the chemical potential in the liquid phase. As already indicated, the model is valid for temperatures from 0 to 260°C and pressures from 0 to 2000 bars. Though the Duan model is developed for calculating the solubility in NaCl solutions up to an ionic strength of 4.5 M, the model is extended to also calculate the solubility of carbon dioxide in more complex solutions containing K^+, Mg^{2+}, Ca^{2+}, and SO_4^{2-}. The final form of the solubility model is

$$\ln m_{CO_2} = \ln y_{CO_2}\varphi_{CO_2}P - \frac{\mu^{l(0)}_{CO_2}}{RT} + 2\lambda_{CO_2-Na}\left(m_{Na}+m_K+2m_{Ca}+2m_{Mg}\right) - \zeta_{CO_2-Na-Cl}m_{Cl}\left(m_{Na}+m_K+m_{Mg}+m_{Ca}\right)+0.07m_{SO_4} \quad (6)$$

Table 3 Measurements of CO_2 solubility			
Authors	Solution	T (°C)	P (bar)
Wiebe & Gaddy (1939)	pure water	50-100	25-700
Wiebe & Gaddy (1940)	pure water	12-40	25-500
Tödheide & Franck (1963)	pure water	50-350	200-3500
Takenouchi & Kennedy (1964)	pure water	110-350	100-1500
King et al. (1992)	pure water	15-40	60-240
Teng et al. (1997)	pure water	5-20	64.4-295
Markham & Kobe (1941)	0-4M NaCl & KCl	0.2-40	1
Harned & Davis (1943)	0-3M NaCl	0-50	1
Ellis & Golding (1963)	0-2M NaCl	170-330	15.7-91.9
Takenouchi & Kennedy (1965)	1.09-4.28M NaCl	150-450	100-1400
Malinin & Savelyeva (1972)	0-4.5 M NaCl & $CaCl_2$	25-75	48
Malinin & Kurovskaya (1975)	0-7M NaCl & $CaCl_2$	25-150	48
Nighswander et al. (1989)	0-0.17M NaCl	80-200	20-100
Rumpf et al. (1994)	4-6M NaCl	40-160	1.5-100
Kiepe et al. (2002)	0-4M NaCl & KCl	40-80	0-100
Bando et al. (2003)	0-0.53M NaCl	30-60	100-200
Yasunishi & Yoshida (1979)	0 – 5M NaCl, KCl, $CaCl_2$, $MgCl_2$	15-35	1
Prutton & Savage (1945)	0-3.9M $CaCl_2$	75-120	15-875
Malinin (1959)	0-1.01M $CaCl_2$	200-350	98.1-490.5
Stewart & Munjal (1970)	synthetic sea water	-5-20	10-45
Portier & Rochelle (2005)	synthetic Utsira pore water	18-80	80-120

where φ_{CO2} is the fugacity coefficient of carbon dioxide, which is a function of temperature and pressure (Duan et al., 2005), and is described as

$$\begin{aligned}\varphi_{CO_2} &= b_1 + \left[b_2 + b_3 T + b_4 / T + b_5 / (T - 150)\right] P + \left[b_6 + b_7 T + b_8 / T\right] P^2 \\ &+ \left[b_9 + b_{10} T + b_{11} / T\right] \ln P + \left[b_{12} + b_{13} T\right] / P + b_{14} / T + b_{15} T^2\end{aligned} \quad (7)$$

The parameters b_i were fitted to six different PT-ranges (Table 4, Fig. 5 (Duan et al., 2005)) in order to make an accurate calculation of φ_{CO2} possible. The quantity y_{CO2} is the mole fraction of CO_2 in the vapour phase, and, by assuming that the vapour pressure of water in the mixture does not differ from the pure water saturation pressure, can be calculated as follows

$$y_{CO_2} = \left(P - P_{H_2O}\right) / P \quad (8)$$

Following Duan et al. (2003), the water vapour pressure can be calculated using the following equation

$$P_{H_2O} = \left(\frac{P_{c,H_2O} T}{T_{c,H_2O}}\right)\left[1 - 38.640844(-t)^{1.9} + 5.8948420t + 59.876516t^2 + 26.654627t^3 + 10.637097t^4\right] \quad (9)$$

where $t = (T\text{-}T_c)/T_c$.

In the solubility equation, λ and ζ are second- and third-order interaction parameters, and $\mu_{CO2}^{l(0)}/RT$ is the standard chemical potential, with R = 0.08314467 bar l/mol K. All three parameters are dependent on temperature and pressure, *par(T,P)* with *par* being λ, ζ, or $\mu_{CO2}^{l(0)}/RT$, and are described by the following equation

$$\begin{aligned}par(T,P) &= c_1 + c_2 T + c_3 / T + c_4 T^2 + c_5 / (630 - T) + c_6 P + c_7 P \ln T \\ &+ c_8 P / T + c_9 P / (630 - T) + c_{10} P^2 / (630 - T)^2 + c_{11} T \ln P\end{aligned} \quad (10)$$

The coefficients to calculate the interaction parameters are shown in Table 5.

Table 4 The parameter coefficients for equation 7

	T-P range					
	1	2	3	4	5	6
b_1	1.0	$-7.1734882\cdot10^{-1}$	$-6.5129019\cdot10^{-2}$	5.0383896	-16.063152	$-1.5693490\cdot10^{-1}$
b_2	$4.7586835\cdot10^{-3}$	$1.5985379\cdot10^{-4}$	$-2.1429977\cdot10^{-4}$	$-4.4257744\cdot10^{-3}$	$-2.7057990\cdot10^{-3}$	$4.4621407\cdot10^{-4}$
b_3	$-3.3569963\cdot10^{-6}$	$-4.9286471\cdot10^{-7}$	$-1.1444930\cdot10^{-6}$			$-9.1080591\cdot10^{-7}$
b_4	0.0			1.957233	$1.4119239\cdot10^{-1}$	
b_5	-1.3179396					
b_6	$-3.8389101\cdot10^{-6}$	$-2.7855285\cdot10^{-7}$	$-1.1558081\cdot10^{-7}$	$2.4223436\cdot10^{-6}$	$8.1132965\cdot10^{-7}$	$1.0647399\cdot10^{-7}$
b_7		$1.1877015\cdot10^{-9}$	$1.1952370\cdot10^{-9}$			$2.4273357\cdot10^{-10}$
b_8	$2.2815104\cdot10^{-3}$			$-9.3796135\cdot10^{-4}$	$-1.1453082\cdot10^{-4}$	
b_9				-1.5026030	2.3895671	$3.5874255\cdot10^{-1}$
b_{10}				$3.0272240\cdot10^{-3}$	$5.0527457\cdot10^{-4}$	$6.3319710\cdot10^{-5}$
b_{11}				-31.377342	-17.763460	-249.89661
b_{12}		-96.539512	-221.34306	-12.847063	985.92232	
b_{13}		$4.4774938\cdot10^{-1}$				
b_{14}		101.81078	71.820393			888.76800
b_{15}		$5.3783879\cdot10^{-6}$	$6.6089246\cdot10^{-6}$	$-1.5056648\cdot10^{-5}$	$-5.4965256\cdot10^{-7}$	$-6.6348003\cdot10^{-7}$

1: 273K < T < 573K, P < P_1 (when T < 305K, $P_1 = P_{sat,CO2}$; when 305K < T < 405K, $P_1 = 75 + (T - 305) \times 1.25$; when T > 405K, P_1 = 200 bar); 2: 273K < T < 340K, P_1 < P < 1000 bar; 3: 273K < T < 340K, P > 1000 bar; 4: 340K < T < 435K, P_1 < P < 1000 bar; 5: 340K < T < 435K, P > 1000 bar; and 6: T > 435K, P > P_1 (also see Fig. 19).

3.3 Comparing the model with experimental data

In Fig 6, available experimental data, together with the model, are plotted as a function of temperature (Fig. 6a), pressure (Fig. 6b), and salinity (Fig. 6c). The following effects of temperature, pressure and salinity on the solubility of CO_2 can be observed

- The solubility of carbon dioxide in solution decreases with increasing temperature, at temperatures below ~100°C, at constant pressure and salinity. When the temperature is above this value the solubility increases again with temperature.
- With increasing pressure, at constant temperature and salinity, the solubility of CO_2 in solution increases. This pressure effect diminishes with increasing pressure, so at lower pressures the solubility increases more rapidly than at higher pressures, as a function of pressure.
- The addition of salt to solution leads to the decrease of carbon dioxide solubility. The magnitude of this effect is determined by the composition of the salt; monovalent salt solutions, e.g. NaCl or KCl, inhibit CO_2 dissolution more than divalent salt solutions, e.g. $CaCl_2$ or $MgCl_2$.

It should be noted that among, the monovalent salts, NaCl seems to inhibit CO_2 solubility more than KCl. This discrepancy is not observed between different divalent chloride salts and sulphate salts. In order to extent the model to more complex systems, containing e.g. Ca^{2+}, Mg^{2+}, K^+, and SO_4^{2-}, an approximation was made. This approximation entails that interaction parameters of equally charged ions have approximately the same value. So binary CO_2-monovalent cation and CO_2-divalent cation interaction parameters are approximated as $\lambda_{CO2\text{-}Na}$ and $2\lambda_{CO2\text{-}Na}$, respectively. CO_2-anion interaction parameters are considered to be small, and hence are neglected. Though, these approximations are considered to be valid, they do not introduce the nature of the separate

Table 5 Interaction parameters for equation 10

	$\mu_{CO2}^{l(0)}/RT$	$\lambda_{CO2\text{-}Na}$	$\zeta_{CO2\text{-}Na\text{-}Cl}$
c_1	28.9447706	-0.411370585	$3.6389723\cdot10^{-4}$
c_2	-0.0354581768	$6.07632013\cdot10^{-4}$	$-1.98298980\cdot10^{-5}$
c_3	-4770.67077	97.5347708	
c_4	$1.02782768\cdot10^{-5}$		
c_5	33.8126098		
c_6	$9.04037140\cdot10^{-3}$		
c_7	$-1.14934031\cdot10^{-3}$		
c_8	-0.30745726	-0.0237622469	$2.12220830\cdot10^{-3}$
c_9	-0.0907301486	0.0170656236	$-5.24873303\cdot10^{-3}$
c_{10}	$9.32713393\cdot10^{-4}$		
c_{11}		$1.41335834\cdot10^{-5}$	

electrolytes. It appears that, hence, the model cannot accurately describe the effect of KCl on the solubility of carbon dioxide.

As can clearly be seen in Fig. 6, experimental data fit reasonably well with the model of Duan et al. (2003; 2005) (average error is less than 7%), though at higher pressures the model deviates more from the experimental data, up to 30%.

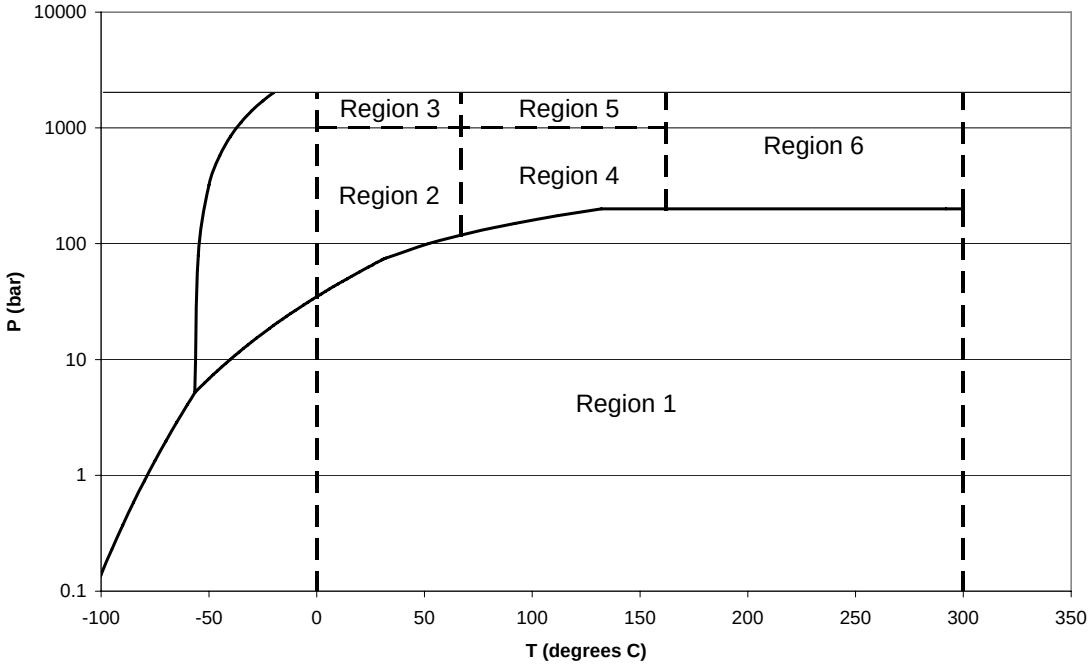

Fig. 5 The six PT-ranges for which the b_i parameters (Table 4) of Eq. 7 will apply. The regions are defined as follows: 1: 273K < T < 573K, P < P_1 (when T < 305K, $P_1 = P_{sat,CO2}$; when 305K < T < 405K, $P_1 = 75 + (T - 305) \times 1.25$; when T > 405K, P_1 = 200 bar); 2: 273K < T < 340K, P_1 < P < 1000 bar; 3: 273K < T < 340K, P > 1000 bar; 4: 340K < T < 435K, P_1 < P < 1000 bar; 5: 340K < T < 435K, P > 1000 bar; and 6: T > 435K, P > P_1 (Duan et al., 2005).

4. Preliminary model: CO_2 sequestration in feldspathic sandstones

In our previous report (Hangx, 2005), a model was developed to predict the rate and extent of carbonate precipitation, on the basis of the data available in the literature. That model has been revised in this report, and a time dependence of grain diameter due to dissolution is incorporated into the existing equations. In addition, a simple model has been developed that predicts rough constraints on the porosity and permeability changes as a result of reaction. Again, we will restrict ourselves to anorthite-rich sandstone, as this is the mineral of main interest in the initial stages of the project

4.1 The precipitating phases

The main CO_2 fixing reactions expected when CO_2 is injected into impure wet sandstones can be summarised by a number of serial and parallel reactions, as shown in Fig. 7. The rate-limiting step in such serial-parallel reaction sequences will in general be the slowest step of the fastest parallel branch. Amongst the above reactions, it is well established in the literature that the silicate dissolution reactions are likely to be the slowest and hence most important in controlling reaction progress (Knauss & Wolery, 1986; Blum & Lasaga, 1988; Casey et al., 1991; Amrhein & Suarez, 1992; Hellmann, 1994; Oxburgh et al., 1994; Ganor et al., 1995; Zysset & Schindler, 1996; Bauer & Berger, 1998; Berg & Banwart, 2000; Cama et al., 2000; Hamilton et al., 2001; Huertas et al., 2001; Köhler et al., 2003). However, it should also be noted that in some cases precipitation reactions might be the slowest! The precipitation of calcite is generally fast, in the order of 10^{-6} mol/m^2 s, at 100°C, 100 bars CO_2 pressure and near neutral pH (Shiraki & Brantley, 1995). Therefore, the precipitation rate of calcite is most likely not rate-controlling; however, the precipitation rate of clays is generally very slow. At 80°C and pH 3, the precipitation rate of gibbsite and kaolinite are 1 to 4 orders of magnitude slower than the dissolution rate of feldspar under the same conditions, respectively (Nagy & Lasaga, 1992, 1993).

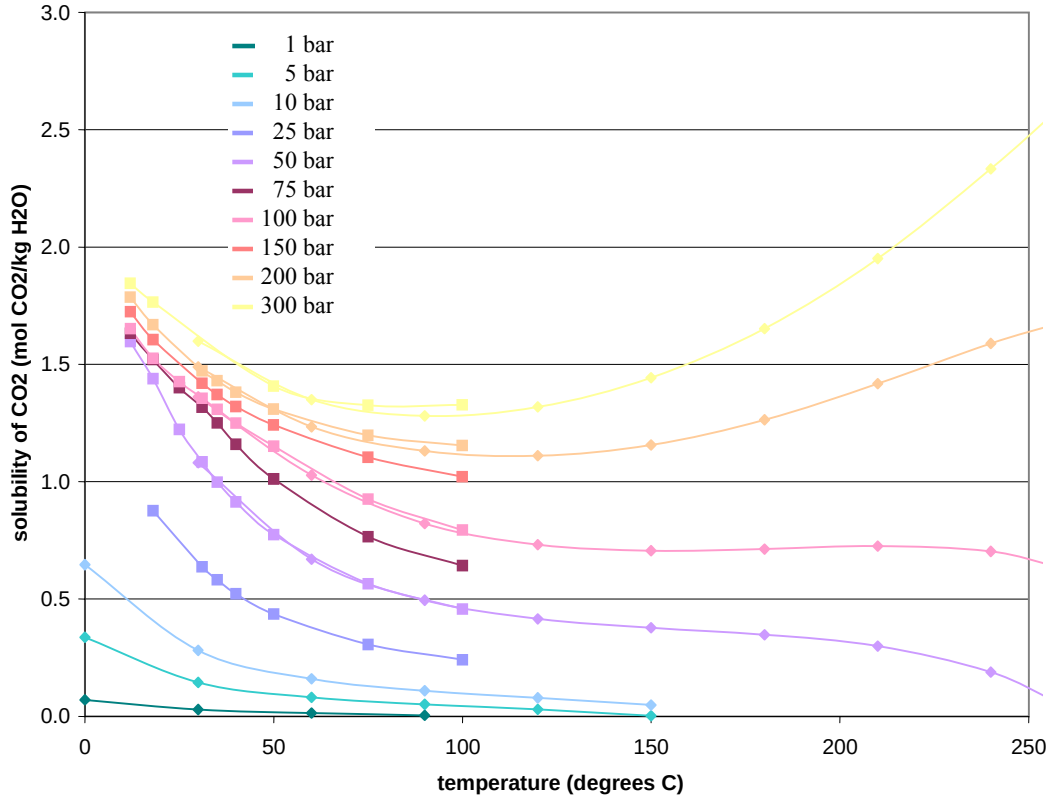

Fig. 6a CO_2 solubility as a function of temperature. ♦ Duan and Sun (2003); ■ Wiebe & Gaddy (1939, 1940).

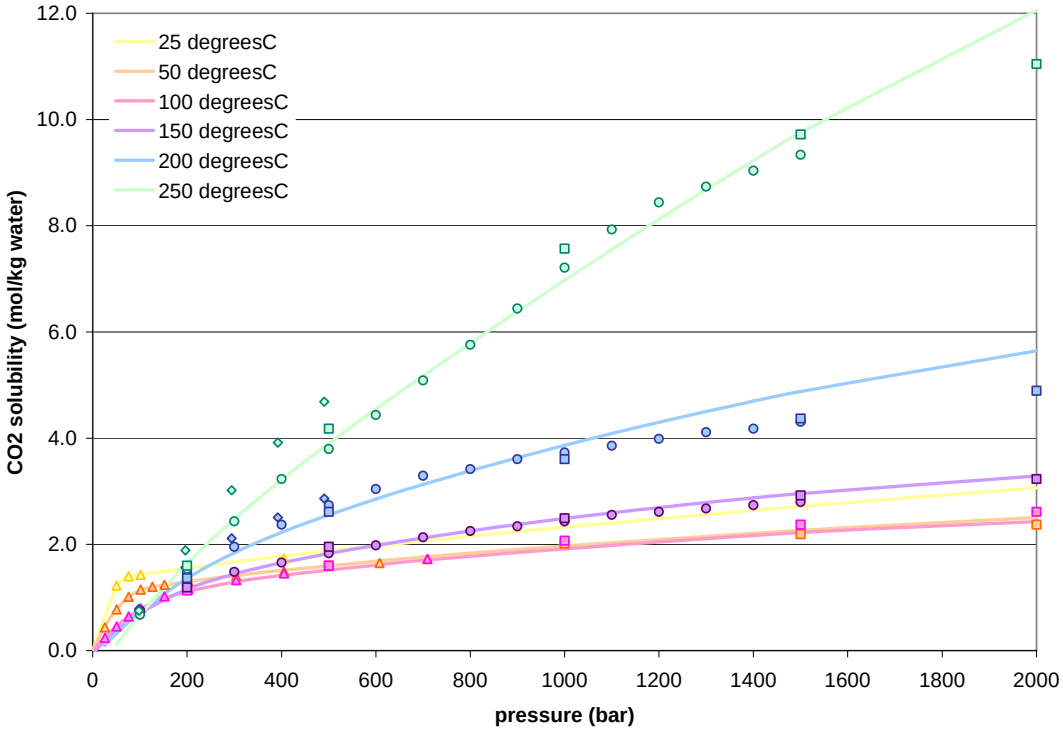

Fig. 6b CO_2 solubility as a function of pressure. Comparison of the model by Duan and Sun (2003, 2005) with experimental data. ▲ Wiebe and Gaddy (1939, 1940); ■ Todheide and Franck (1963); ● Takenouchi and Kennedy (1964); ♦ Malinin (1959).

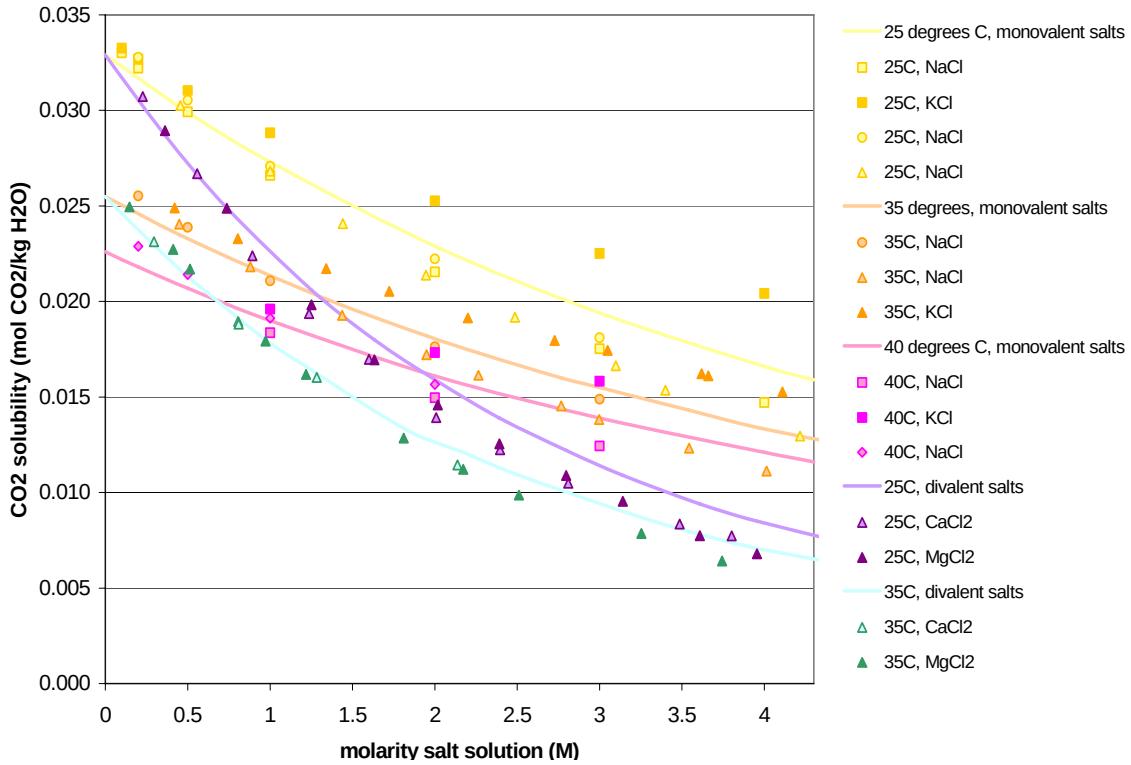

Fig. 6c CO_2 solubility as a function of molarity, at 1 atm pressure. Comparison of the model by Duan and Sun (2003, 2005) with experimental data. ■ Markham and Kobe (1941); ♦ Harned and Davis (1943); ▲ Yasunishi & Yoshda (1979).

The following consists of a short overview of the kinetics of clay mineral precipitation. Though, in the literature, more attention is paid to the dissolution kinetics of clay minerals, a few studies have been done on the precipitation kinetics of kaolinite and gibbsite. These studies (Nagy & Lasaga, 1992, 1993; Devidal et al., 1997) have already shown that the precipitation of gibbsite is much faster than the precipitation of kaolinite, which may vary by 3 orders of magnitude, as shown in Fig. 8.

Precipitation of both minerals depends on chemical affinity, or solution saturation state, especially when approaching equilibrium. Though Si and Al ions in solution may inhibit clay dissolution, they enhance precipitation. It is generally agreed that Transition State Theory can describe these effects on the precipitation of kaolinite and gibbsite (Nagy & Lasaga, 1992, 1993; Devidal et al., 1997) as follows

$$gibbsite:\ R_{precipitation} = -(2.07 \pm 0.63)\cdot 10^{-10}\left[1 - \exp\left(\frac{|\Delta G_r|}{RT}\right)^{(1.20\pm 0.31)}\right] \qquad (11a)$$

$$kaolinite:\ R_{precipitation} = (3.4 \pm 0.91)\cdot 10^{-13}\left[1 - \exp\left(\frac{(-1.9 \pm 1.4)\,|\Delta G_r|}{RT}\right)\right] \qquad (11b)$$

where the precipitation rate $R_{precipitation}$ is in mol/m^2 s, R = 8.3145 J/mol K, T is absolute temperature in K, and ΔG_r is the deviation of the Gibbs free energy of the reaction [kcal/mol]. For gibbsite ΔG_r may vary over the range $0 \le \Delta G_r \le 0.467$ kcal/mol (Nagy & Lasaga, 1992), and for kaolinite $0 \le \Delta G_r \le 1.11$kcal/mol (Nagy & Lasaga, 1993). Not much is known about the actual mechanism of precipitation but it is agreed that surface roughness may affect the rate of precipitation (Nagy & Lasaga, 1992, 1993) and that, during simultaneous precipitation, gibbsite and kaolinite will precipitate only on itself (Nagy & Lasaga, 1993).

a. CO_2 mineralisation via anorthite dissolution

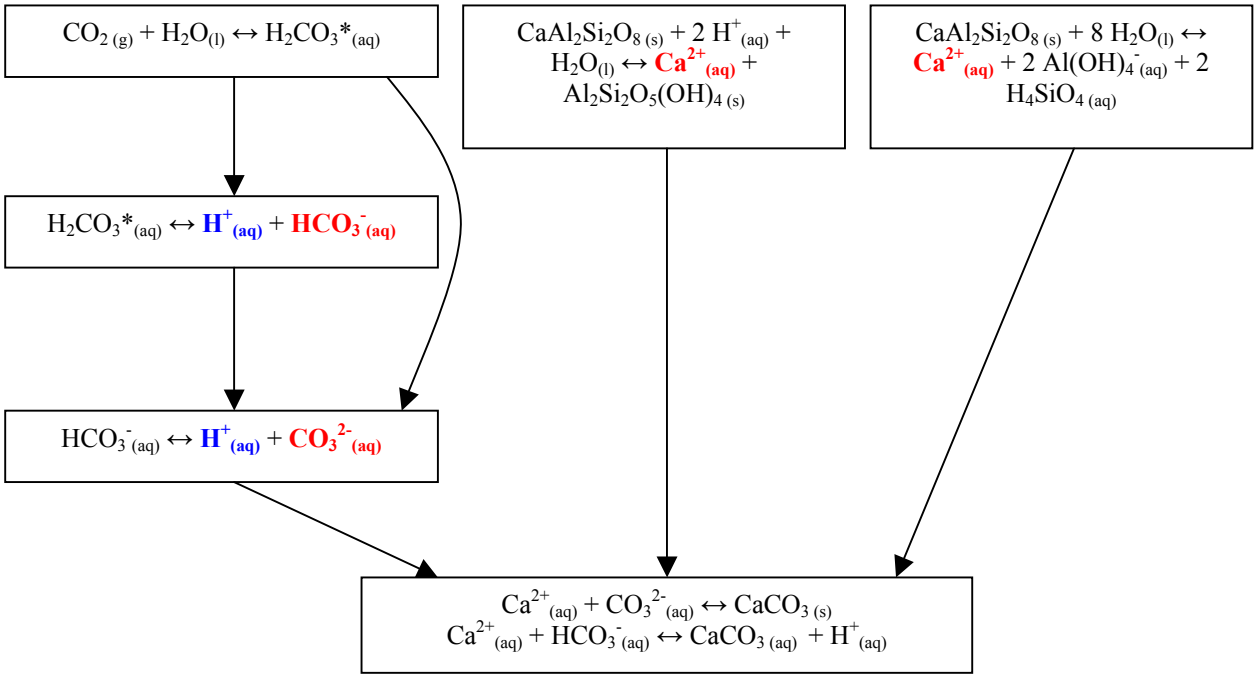

b. CO_2 mineralisation via Ca-rich clay dissolution

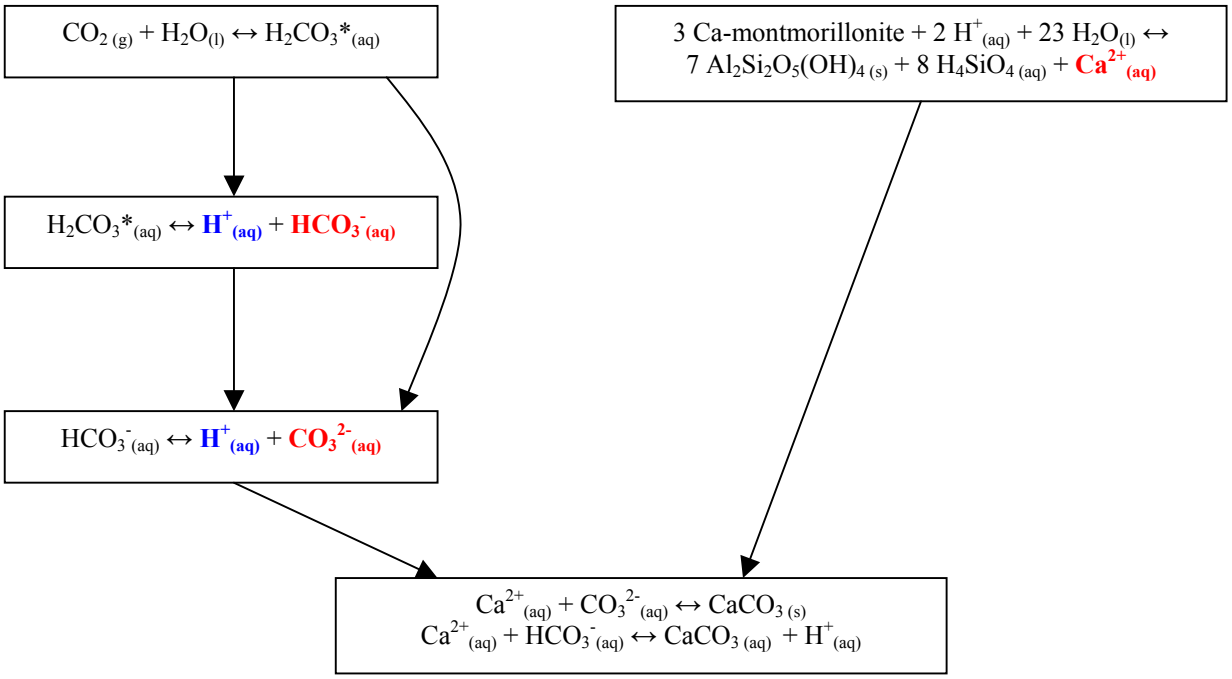

Fig. 7 Reaction schemes showing (a) the serial and parallel reactions occurring during the dissolution of anorthite; and, (b) the serial and parallel reactions occurring during the dissolution of Ca-rich clay. In both cases, the protons formed by the CO_2-dissolution-branch (blue) will attack the anorthite and clay, resulting in the release of Ca^{2+}-ions. The calcium and bicarbonate or carbonate ions from the parallel branches (red) will together result in the precipitation of calcite.

4.2 Conditions allowing calcite precipitation

The precipitation of calcite, or other carbonates, is limited by various conditions: (1) the anorthite content; (2) the water content; and, (3) the carbon dioxide pressure. It is safe to assume that CO_2 will be added in sufficient amounts and therefore, the extent of CO_2 sequestration will depend on the availability of anorthite and water. When either one of the two runs out, the process will come to a halt and a new equilibrium will be established. However, excess carbon dioxide will strongly influence this equilibrium, or even already the precipitation of carbonate, as the dissolution of carbon dioxide results in acidification of the system. When the acidity is too high, calcite will dissolve again when the sequestration process comes to a halt, or, it may even not precipitate at all, if the driving force for precipitation cannot overcome that for dissolution. In the future a careful analysis of the chemical system will be made in order to identify the range of conditions in which calcite precipitation can take place.

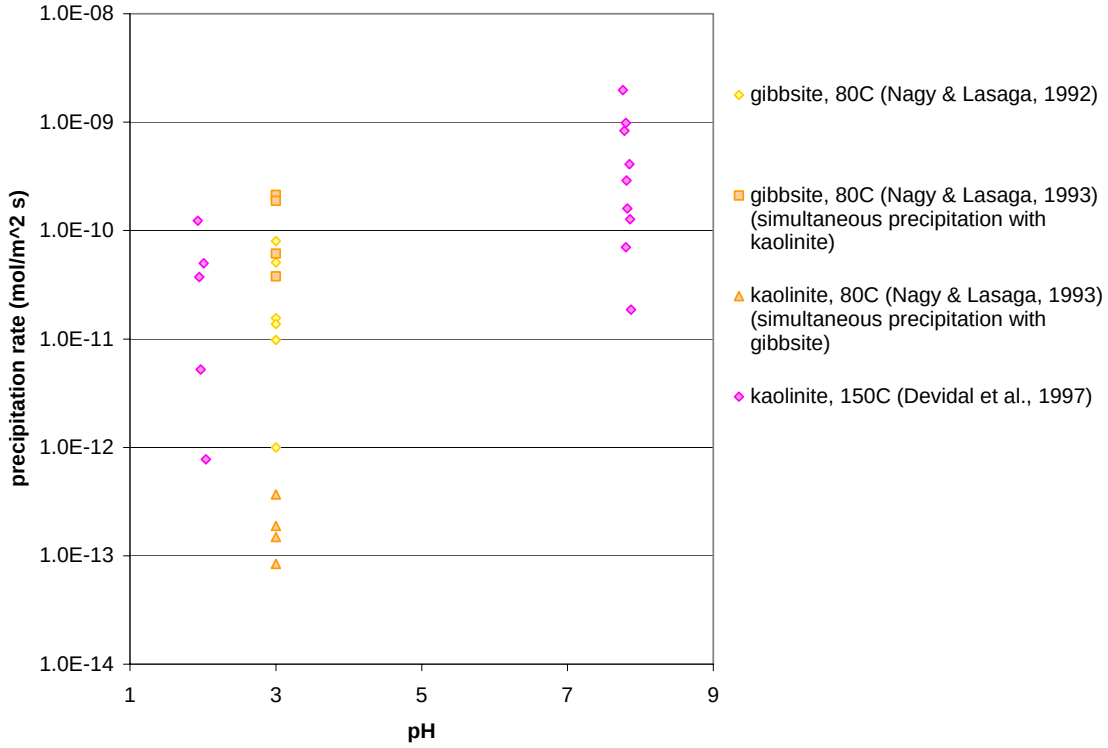

Fig. 8 Clay mineral precipitation rate as a function of pH, and temperature. *(after Nagy and Lasaga (1992), Nagy and Lasaga (1993), and Devidal et al. (1997)).*

4.3 Likely rate-limiting step in CO_2 sequestration

Predictions have been made, in the literature and by the author (Hangx, 2005), on the expected order of magnitude of the reaction rate, which depends on the rate-limiting step in the system. The precipitation of carbonate relies on the availability of Ca^{2+} and CO_3^{2-}, or HCO_3^-, which in turn relies on the dissolution of feldspar, the calcium source, and the dissolution of CO_2, which provides the carbonate or bicarbonate ions, as schematically shown in Fig. 1a. All of the steps, shown in Fig. 1a, either for the dissolution of CO_2 or the dissolution of feldspar, can be rate-limiting, including the precipitation of carbonates or clays. Previous experiments with CO_2 (Czernichowski-Lauriol et al., 1996) have shown that the dissolution of carbon dioxide at high pressure is a rather fast process, therefore, the formation of CO_3^{2-} and HCO_3^- is not considered to be rate limiting. However, it is possible that carbon dioxide dissolution, in reservoir water, is rate limiting, as the contact area of the carbon dioxide with the pore water is significantly different in nature compared with a laboratory set-up. In a laboratory set-up, CO_2 can usually dissolve into the reacting fluid across a fairly large contact area, which makes it possible for dissolution to be fast. However, in a reservoir the dissolution of

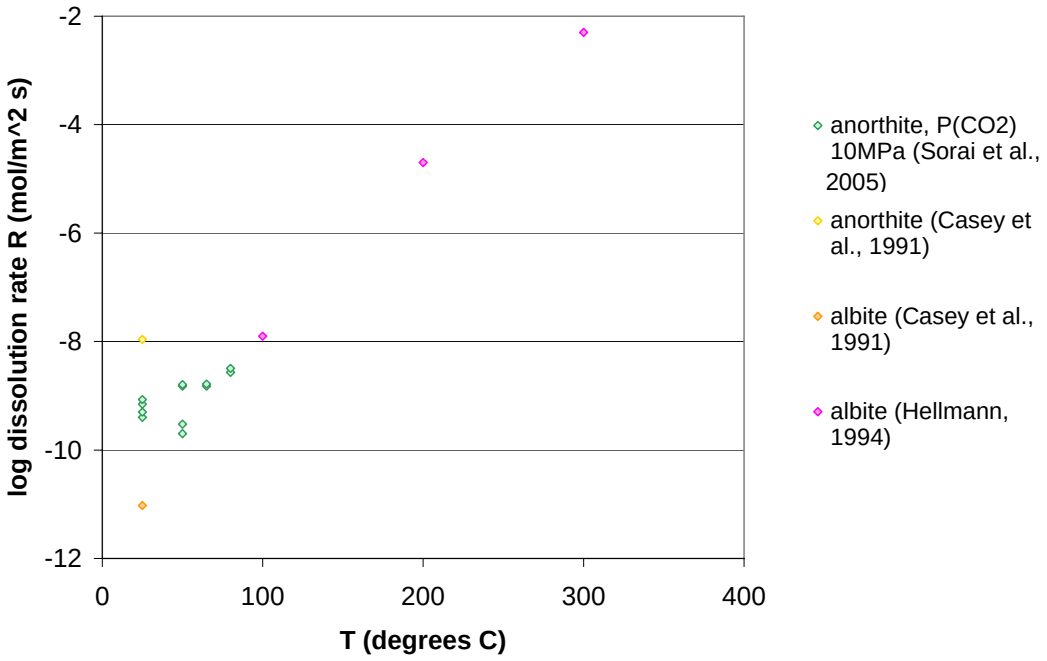

Fig. 9 Comparison between the dissolution rates of albite and anorthite at various temperatures, at pH ~ 3 *(after Sorai et al., 2005)*.

carbon dioxide can be rate-limiting in various ways, mainly as an effect of the contact area between the gas phase and the fluid phase: (1) pores are only partially filled with water, which makes it easy for the CO_2 to spread through the system, though only a little CO_2 can dissolve at a time; (2) the pores are completely filled with water, which prevents the CO_2 from entering the pores and dissolve there, but instead it dissolves at the injection well and diffuses its way through the system; and, (3) CO_2 spreads through the system parallel to fractures, or layering, and diffusion controls further spreading. However, order of magnitude calculations indicate that CO_2 will generally be rapid, so for now it is assumed that carbon dioxide dissolution is not the rate-limiting step in the process, which leaves us with the dissolution of feldspar or the precipitation of carbonates and clays as possible rate-limiting step(s). As stated earlier, the precipitation rate of calcite in pure water is fast (Shiraki & Brantley, 1995) compared to the dissolution rate of silicate minerals, and certainly faster than the precipitation rate of clay minerals, like kaolinite and gibbsite. Therefore, carbonate precipitation as the rate-limiting step is unlikely. That leaves us with either feldspar dissolution or clay precipitation as the rate-limiting step in CO_2 mineralisation of feldspars. However, it should be noted that, the presence of Mg^{2+} or PO_4^{3-} ions in solution, which is likely in reservoir pore waters, inhibit the precipitation of calcite (Zhang & Spiers, 2005). In this case calcite precipitation may become rate-limiting.

At a CO_2 pressure of 15 MPa we calculated that the pH of the pore water would be ~ 3.1, and would not differ much over a considerable temperature range. Sorai et al. (2005) obtained similar values for solution pH, 3.1 to 3.2, at temperatures of 25° to 80°C, and at a $P(CO_2)$ of 10 MPa. Using the calculated value for the pH plus the reaction rate equations of Casey et al. (1991) and Hellmann (1994) (equations 18a and 29, App. 3b), the dissolution rates of albite and anorthite were calculated at various temperatures and compared to those obtained in other dissolution experiments at elevated CO_2 pressure (Sorai et al., 2005) (Fig. 9). In the temperature range 25° to 100°C the dissolution rate of feldspar, at pH 3, will be in the order of 10^{-9} to 10^{-8} mol/m^2 s, in pure water.

Another argument for using the rates obtained by Sorai et al. (2005) is that they most likely measured the actual rate of reaction (3), since they measured the dissolution rate of an anorthite crystal at various temperatures and a P_{CO2} of 100 bars. However, the limited time period of one week probably produced only a very small amount of precipitate, which might mean that the solution phase never became supersaturated with respect to precipitating phases. This may also explain the different value for the activation energy, 6 kJ/mol, they obtained, compared to other values for anorthite dissolution, i.e. 18.4 kJ/mol (Oelkers & Schott, 1995). Therefore, we predict that the overall reaction rate of reaction (3) will be in the order of 10^{-8} to 10^{-9} mol/m^2 s.

4.4 Preliminary model for CO_2 fixation in feldspathic sandstone

The data presented above can be used to derive equations that relate

- the overall reaction rate to the rate of carbonate precipitation per cubic meter of feldspar-rich sandstone rock per second,
- the total amount of carbonate formed to the available amount of anorthite, or water content, and
- the total amount of precipitate per cubic meter of impure sandstone to porosity and permeability changes in the rock

In order to do so, several assumptions have to be made: (1) all feldspar dissolves into the pore water; and, (2) the rate of CO_2 dissolution is not influenced by the contact area of carbon dioxide with the pore fluid.

4.4.1 Rate of carbonate precipitation

Consider a cubic meter of anorthite-rich sandstone rock with a given porosity φ, a constant grainsize d, and containing X volume-% of anorthite. Reaction of this rock with CO_2 can be described by the following reaction

$$CaAl_2Si_2O_{8\,(s)} + CO_{2\,(g)} + 2\,H_2O_{(l)} \leftrightarrow CaCO_{3\,(s)} + Al_2Si_2O_5(OH)_{4\,(s)} \qquad (3)$$

The reaction rate of this reaction is given as follows

$$R = k_+ a_{\text{anorthite}} a_{CO_2} a_{H_2O}^2 - k_- a_{\text{calcite}} a_{\text{kaolinite}} \qquad [\text{mol/m}^2\text{s}] \qquad (12)$$

where, k_+ and k_- are the forward and backward reaction rate constants, respectively, and a_i is the activity of species i. The reaction rate predicts that the amount of carbonate formed depends on the total grain surface area of anorthite involved in reaction. The change in total grain surface area of anorthite, A_s, per m^3 of sandstone rock, as a function of time, is given as

$$A_s(t) = N_{\text{grains}}\, A_{\text{grain}}(t) \qquad [\text{m}^2/\text{m}^3] \qquad (13)$$

where, N_{grains} is the number of anorthite grains present per unit volume of rock, and A_{grain} is the change of surface area of one grain with time [m^2/s]. The number of anorthite grains in one unit volume of rock can be calculated from the volume-% of anorthite present in the rock. Assuming that all grains are spherical and of equal size N_{grains} can be expressed as

$$N_{\text{grains}} = 6 \cdot 10^{15} \left(\frac{m_{\text{anorthite}}}{\pi \rho_{\text{anorthite}} d^3} \right) \qquad [\text{m}^{-3}] \qquad (14)$$

where, $m_{\text{anorthite}}$ is the total mass of anorthite present in a unit volume of sandstone rock [kg], $\rho_{\text{anorthite}}$ is the density of anorthite [g/cm^3], and d is the grain size [μm]. The mass of anorthite per unit volume is related to the vol.-%, or actually the volume fraction, of anorthite in the sandstone:

$$m_{\text{anorthite}} = 10\, \rho_{\text{anorthite}} X \qquad [\text{kg/m}^3] \qquad (15)$$

The grain size of anorthite changes with time, as a results of dissolution, and can be described as

$$d(t) = 5 \cdot 10^{-13}\, d_0 - R\, \Omega\, t \qquad (16)$$

where, d_0 is the initial grain size [μm], R is the dissolution rate of anorthite [mol/m^2 s], Ω is the molar volume of anorthite [cm^3mol], and t is time [s]. Now the change of total anorthite surface area with time can be expressed as

$$A_s(t) = 4\pi N_{\text{grains}} (5 \cdot 10^{-12}\, d_0^2 - 10^{-6}\, R\, \Omega\, d_0\, t + R^2 \Omega^2 t^2) \qquad (17)$$

The reaction rate predicts that per m^2 of anorthite surface area R moles of Ca^{2+} are released per second. In turn, each mole of Ca^{2+} converts to 1 mole of carbonate. Therefore, the amount of carbonate produced per unit volume of sandstone rock per second, $\dot{M}$, can be described as

$$\dot{M} = \frac{\mathrm{R\ A_s}(t)\, m_{\mathrm{calcite}}}{1000} \qquad [\mathrm{kg/m^3 s}] \tag{18}$$

where, m_{CaCO3} is the molar mass of calcite [g/mol].

The only variable left is the total surface area of anorthite involved in reaction, which, in turn, is related to the reactive surface area of each anorthite grain. There are two end-member models to predict the surface area involved in reaction per grain. The maximum surface area model assumes that the whole surface of the grain, including the grain-to-grain contacts, is active during reaction

$$\mathrm{A_{grain,\ max}}\ (t) = 10^{-12}\ \pi\ d(t)^2 \qquad [\mathrm{m^2}] \tag{19}$$

In contrast, the minimum surface area model assumes that the area at grain-to-grain contacts is excluded from reaction. By using a simple grain contact area equation the minimum surface area can be expressed as

$$\mathrm{A_{contact}} = \frac{4\pi r^2}{N}(1-2\varphi) \qquad [\mathrm{m^2}] \tag{20}$$

where, N is the coordination number, and r is the radius of the grains.

$$\mathrm{A_{grain,\ min}} = \mathrm{A_{grain,\ max}} - \mathrm{A_{contact}}$$

$$\mathrm{A_{grain,\ min}} = 10^{-12}\,\pi d(t)^2\left(1-\frac{1-2\varphi}{N}\right) \qquad [\mathrm{m^2}] \tag{21}$$

Now two equations can be derived to quantify the minimum and maximum amount of carbonate that can precipitate in one cubic meter of feldspar-rich sandstone rock per second

$$\dot{M}_{\max} = 60\left(\frac{X\ \mathrm{R}(P_{\mathrm{CO_2}}, T)\, m_{\mathrm{calcite}}}{d(t)}\right) \qquad [\mathrm{kg/m^3 s}]$$

$$\dot{M}_{\min} = 60\left(\frac{X\ \mathrm{R}(P_{\mathrm{CO_2}}, T)\, m_{\mathrm{calcite}}}{d(t)}\right)\left(1-\frac{1-2\varphi}{N}\right) \qquad [\mathrm{kg/m^3 s}] \tag{22a,b}$$

The dependence of the rate of reaction, R, on temperature and pressure, can be expressed as follows:

$$\mathrm{R} = \mathrm{k_+} a_{\mathrm{anorthite}} a_{\mathrm{H_2O}}^2 \phi_{\mathrm{CO_2}} P_{\mathrm{CO_2}} - \mathrm{k_-} a_{\mathrm{calcite}} a_{\mathrm{kaolinite}} \qquad [\mathrm{mol/m^2 s}] \tag{23}$$

and k has a temperature dependence, according to Arrhenius relationship; $\mathrm{k} = Ae^{-\mathrm{E_a}/\mathrm{R}T}$

where, ϕ_{CO_2} is the fugacity coefficient of CO_2, P_{CO_2} is the CO_2 pressure, A is a pre-exponential frequency factor, R is the universal gas constant, E_a is the activation energy for the forward/backward reaction, and T is the temperature.

4.4.2 Extent of calcite precipitation and CO_2 deposition

If the total amount of carbonate, which is formed in one cubic meter of rock, is known the time needed to precipitate that amount can be predicted. The total amount of $CaCO_3$ that can be precipitated depends on the availability of anorthite and the water content of the system, the reaction will come to a halt when either one is depleted. Taking this into account an equation can be derived which can calculate the maximum amount of carbonate that can precipitate, as a function of either the anorthite or water content.

$$M_{\mathrm{T,anorthite}} = \mathrm{N}^{\mathrm{moles}}_{\mathrm{anorthite}} m_{\mathrm{calcite}} = \frac{10\,\rho_{\mathrm{anorthite}}\, m_{\mathrm{calcite}}\, X}{m_{\mathrm{anorthite}}} \qquad [\mathrm{kg/m^3}]$$

$$M_{\mathrm{T,H_2O}} = 0.5\,\mathrm{N}^{\mathrm{moles}}_{\mathrm{water}} m_{\mathrm{calcite}} = \frac{5\,\rho_{\mathrm{H_2O}}\, m_{\mathrm{calcite}}\, W}{m_{\mathrm{H_2O}}} \qquad [\mathrm{kg/m^3}] \qquad (24a,b)$$

where, $M_{\mathrm{T,i}}$ is the total amount of calcite formed per unit volume of sandstone rock, either as a function of anorthite or as a function of water content, $\mathrm{N}^{\mathrm{moles}}$ is the number of moles of water, or anorthite, per unit volume of sandstone rock, ρ_{i} is the density of species *i* [g/cm^3], m_{i} is the molar mass of species *i* [g/mol], and *X* and *W* are the vol.-% of anorthite and water, respectively.

The choice of equation depends on the availability of anorthite and water; the one that runs out first controls the amount carbonate that precipitates. Reaction (3) requires one mole of anorthite and two moles of water to form one mole of calcite, hence the following holds:

$$\text{if, } \frac{\mathrm{N}^{\mathrm{moles}}_{\mathrm{anorthite}}}{\mathrm{N}^{\mathrm{moles}}_{\mathrm{water}}} \geq 0.5 \text{ : the water content limits the amount of calcite formed}$$

$$\text{and if, } \frac{\mathrm{N}^{\mathrm{moles}}_{\mathrm{anorthite}}}{\mathrm{N}^{\mathrm{moles}}_{\mathrm{water}}} \leq 0.5 \text{ : the anorthite content limits the amount of calcite formed}$$

When the ratio is equal to 0.5 both anorthite and water will run out at the same time, and hence, both will be the limiting factor.

This ratio can also be expressed as a function of the anorthite and water content of the sandstone rock:

$$\left(\frac{\rho_{\mathrm{anorthite}}\, m_{\mathrm{water}}}{\rho_{\mathrm{water}}\, m_{\mathrm{anorthite}}}\right)\frac{X}{W} = 0.5 \qquad (25)$$

The density of water varies with pressure and temperature, as can be seen in pressure-temperature-density graphs given in the literature (Fisher, 1976). However, under the conditions considered for CO_2 sequestration (P < 500 bar, T < 100°C) this variation is less than 0.05%. Therefore, the density of water is considered to be constant at a value of 0.98 g/cm^3. The density of anorthite is taken to be 2.75 g/cm^3, the molar masses of water and anorthite are 18.02 g/mol and 277.41 g/mol, respectively. Taking these values into account, the ratio between the anorthite and water content predicts the following:

$$\text{if, } \frac{X}{W} \geq 2.74 \text{ : the water content is the limiting factor} \rightarrow \text{use equation 24b}$$

$$\text{or if, } \frac{X}{W} \leq 2.74 \text{ : the anorthite content is the limiting factor} \rightarrow \text{use equation 24a}$$

By using equations 22 and 24 it is possible to make an estimate of the reaction time of reaction (3), or, in other words, the time it will take for the maximum amount of calcite to be precipitated, and the maximum amount of CO_2 is sequestered as carbonate. Fig. 10 shows the amount of calcite precipitated as a function of time, also shown is the amount of CO_2 fixed by mineralisation. Calculations were made for a sandstone reservoir containing 20 vol-% anorthite, at a temperature of 50°C and P_{CO2} = 100 bar. It can be seen that for this scenario approximately 200 kg of calcite will be formed, per cubic meter of sandstone, and ~ 87 kg of CO_2 will be fixed by mineralisation, per cubic meter of sandstone.

4.4.3 Porosity-permeability evolution of a reservoir

As states earlier, CO_2-rock interaction can be described by reaction (3), the conversion of anorthite into kaolinite and carbonate. Upon reaction a 36.2% volume increase occurs, which, depending on the location of precipitation, may influence the porosity and permeability of the sandstone reservoir to a certain extent. Since porosity and permeability influence the physical properties of the reservoir it is

important to be able to predict the porosity-permeability evolution, as a function of the extent of reaction. In order to do so several assumptions have been made

- the pores are represented by tubes
- all pores are equal and disturbed homogeneously throughout the reservoir
- the reservoir does not deform under the chemical changes occurring

Two models have been derived in order to predict both the minimum and maximum effect of precipitation. In both cases the porosity and permeability have been calculated using equations for a tubes model developed by Guéguen and Palciauskas (1994). The porosity is described as follows

$$\varphi = \frac{10^{-12}\pi r_{pore}^2 D}{L^3} \tag{26}$$

where, r_{pore} is the pore radius [μm], D is the length of a pore, and L is the distance between the pores. It is assumed that both D and L are determined by the sandstone structure, and hence the grain size of the minerals in the reservoir. Since quartz is the main mineral that builds up the reservoir structure, and does not participate in the reaction, i.e. does not dissolve, it is assumed that D and L are equal to the initial grain size.

It is assumed that the permeability is related to the porosity, when, in fact, it is determined by the porosity *microstructure*. However, the empirical law derived for calculating the permeability (Guéguen & Palciauskas, 1994) can satisfactorily predict the permeability, in spite of this assumption

$$k = \frac{10^{-12} r_{pore}^2}{8}\varphi \qquad [\mathrm{m}^2] \tag{27}$$

where, k is the permeability [m^2].

The two models that have been are derived are: (1) the "porous grain" model, and (2) the "shrinking grain" model. The "porous grain" model assumes that the feldspar grains are merely leached, as opposed to actual dissolution. This implies that the anorthite grains remain "porous", and react without

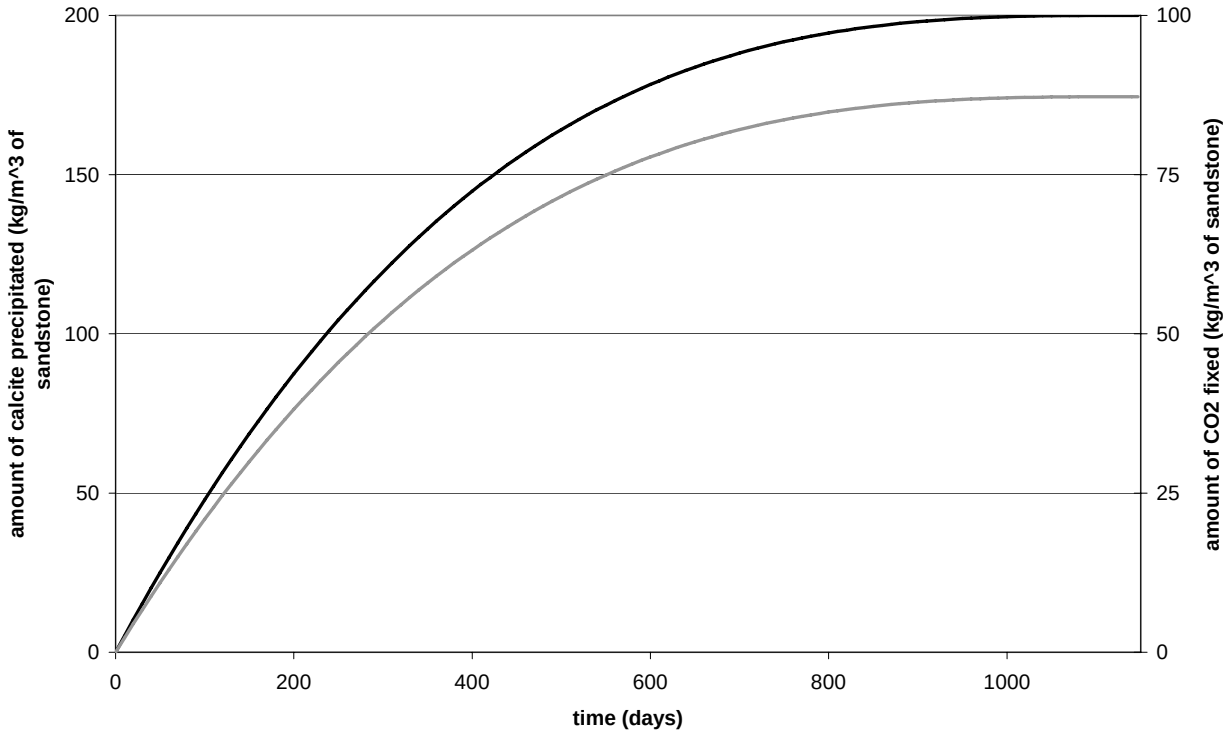

Fig. 10 Extent of calcite precipitation (black line) and CO_2 fixation (grey line), as a function of time, in a sandstone reservoir containing 20 vol-% anorthite. Reaction conditions are 50°C and 100 bars CO_2-pressure.

a

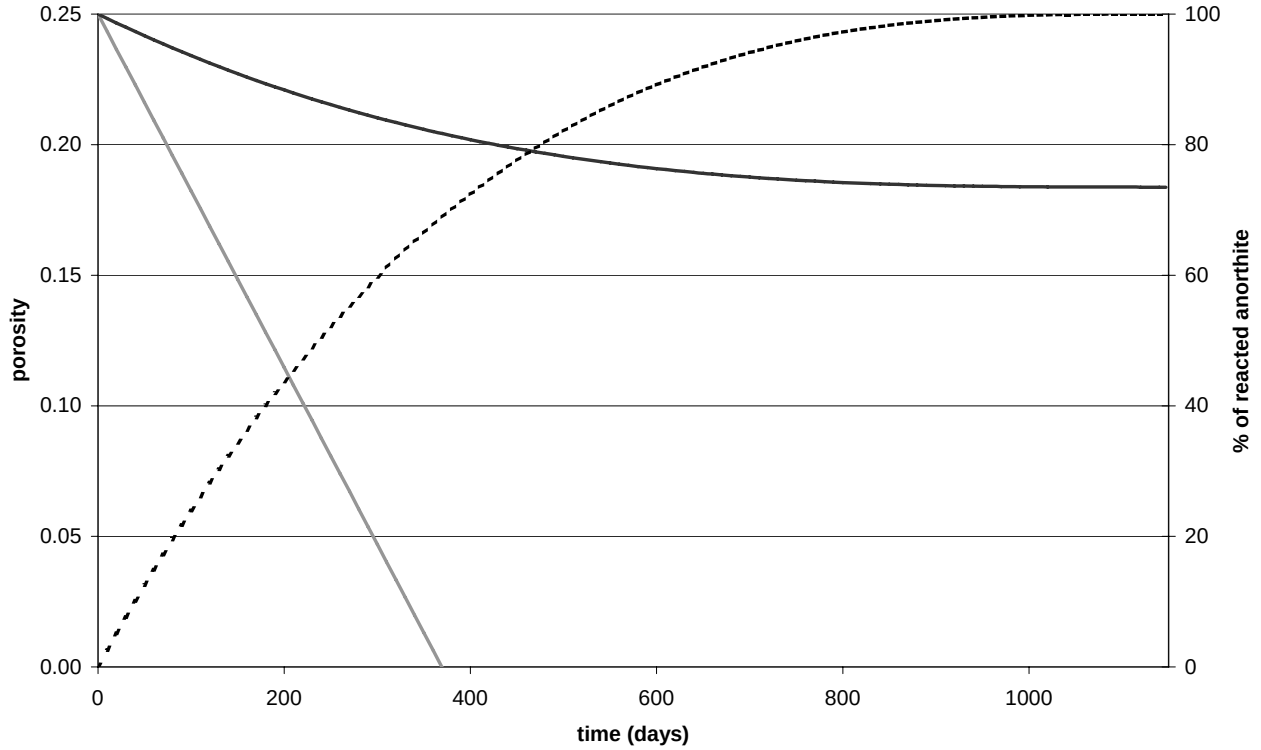

b

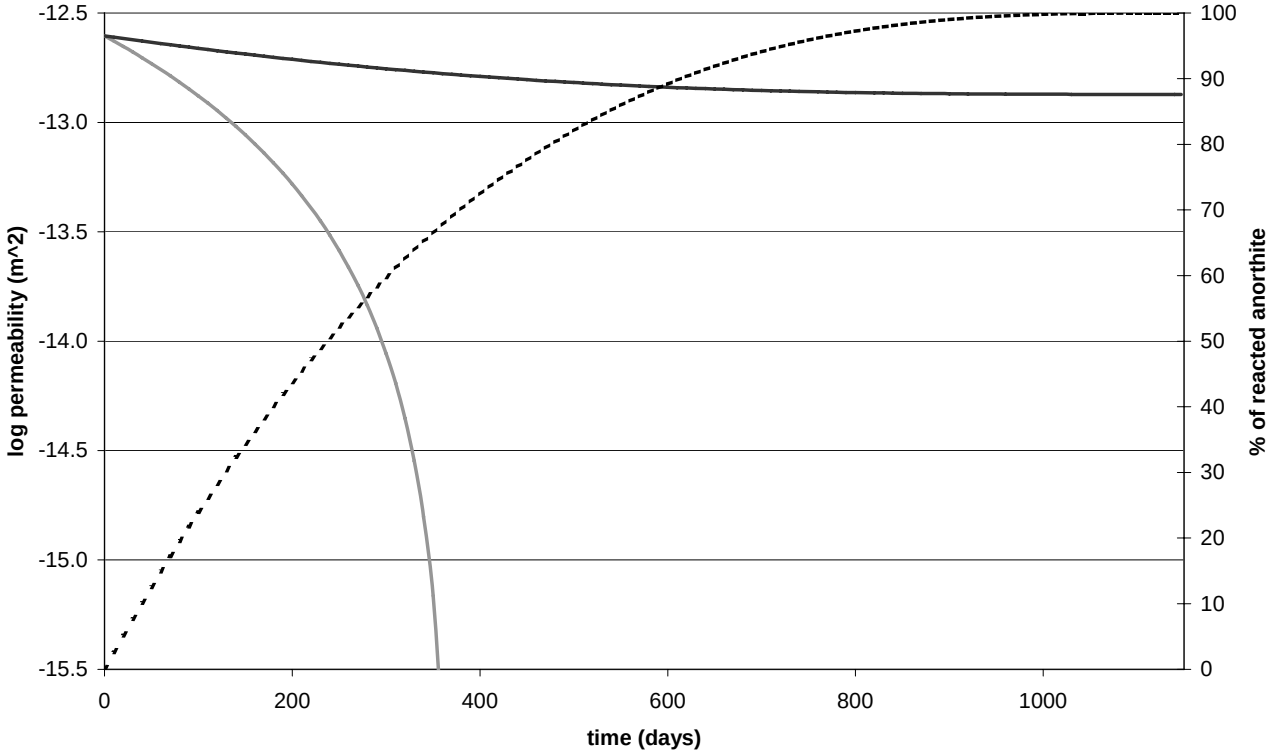

Fig. 11 Porosity-permeability evolution of a sandstone reservoir containing 20% anorthite and a porosity of 25%. Temperature is 50°C and the injected CO_2 pressure is 100 bars. a) Porosity changes as a function of time; b) Permeability changes as a function of time. The dark grey lines represent the "shrinking grain" model, and the light grey lines the "porous grain" model. For comparison also the extent of anorthite dissolution has been plotted (dotted black lines).

loss of their structure and size. As a result all material is precipitated in the pores, and it is assumed that this occurs from the pore wall inward. Figure 11 shows the results of a calculation of the evolution of porosity and permeability with time, and the percentage of reacted anorthite. It is clear that for the "porous grain" model the porosity decreases rapidly, as a result of the large surface area of the grains since the grains do not get smaller. In this case, a sandstone reservoir containing 20% anorthite and an initial porosity of 25% will be clogged up within 360 days. The "shrinking grain" model does take into account the dissolution of the grains, and therefore the changing grain size. As a result of the dissolving anorthite grains the porosity of the rock increases. It is assumed that the precipitating phases first fill up this newly generated pore space and than the remaining pore space, again from the pore wall inward. The "shrinking grain" model affects the porosity of the reservoir to a much smaller extent. The porosity is being reduced by ~ 7% and the reservoir remains highly permeable to fluids, even when all of the feldspar has reacted.

The models presented above give very different results for the porosity-permeability evolution of a reservoir. The "porous grain" model shows a very unfavourable view on the evolution of the reservoir. It would become "impermeable" after perhaps 350-360 days. However, it should be noted that the principle of the model, i.e. constant grain size of the feldspar grains, is very unlikely to occur in nature. A more realistic scenario is that of the "shrinking grain" model, and the actual porosity-permeability evolution of the reservoir will therefore be much closer related to this model than the other.

In summary, the porosity-permeability evolution of a sandstone reservoir is strongly dependent on the mechanism of dissolution, as well as on the location of precipitation. In these two cases a fairly simple assumption has been made, that the precipitate will grow from the pore walls inward, however, growth of minerals in the centre of pores is also possible and will affect the porosity and permeability in a completely different way. More complex models will be considered in the future and subsequently tested against experiments in the later stage of the project.

5. Experiments: design and results to date

As most of the dissolution rates of silicate minerals, stated in the literature, are measured at atmospheric or low carbon dioxide pressures, these equations are not sufficient to make adequate calculations in the experimental range we are interested in. Therefore, various experimental set-ups have been designed in order to determine reaction rates at elevated temperature and carbon dioxide pressure, which are described below. During the first series of experiments that will be performed, the aim is to determine the reaction rate of the following reaction will be determined

$$CaAl_2Si_2O_{8\,(s)} + CO_{2\,(g)} + 2H_2O_{(l)} \leftrightarrow CaCO_{3\,(s)} + Al_2Si_2O_5(OH)_{4\,(s)} \qquad (3)$$

5.1 Effect of environmental variables on the dissolution rate of feldspars

The dissolution rate of feldspars is very slow, on the order of 10^{-10} mol/m^{2}s at room temperature and a pH of 3, or a CO_2 pressure of 100 bars. Under these conditions it would mean that dissolution of an anorthite grain would take years. In order to reduce this to experimental timescales, various variables can be changed in order to speed up the process, namely: (1) temperature; (2) P_{CO2}; and (3) salinity.

5.1.1 Temperature effect on dissolution rate

Temperature is a factor that has a significant effect on the dissolution rate of minerals. Its

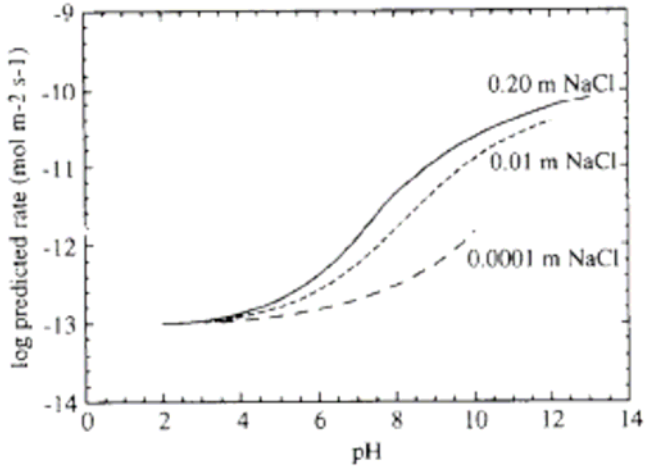

Fig. 12 The predicted dissolution rates of quartz at 25°C as a function of pH. The reaction rate is independent of cation concentration below approximately pH 4 (Dove & Elston, 1992).

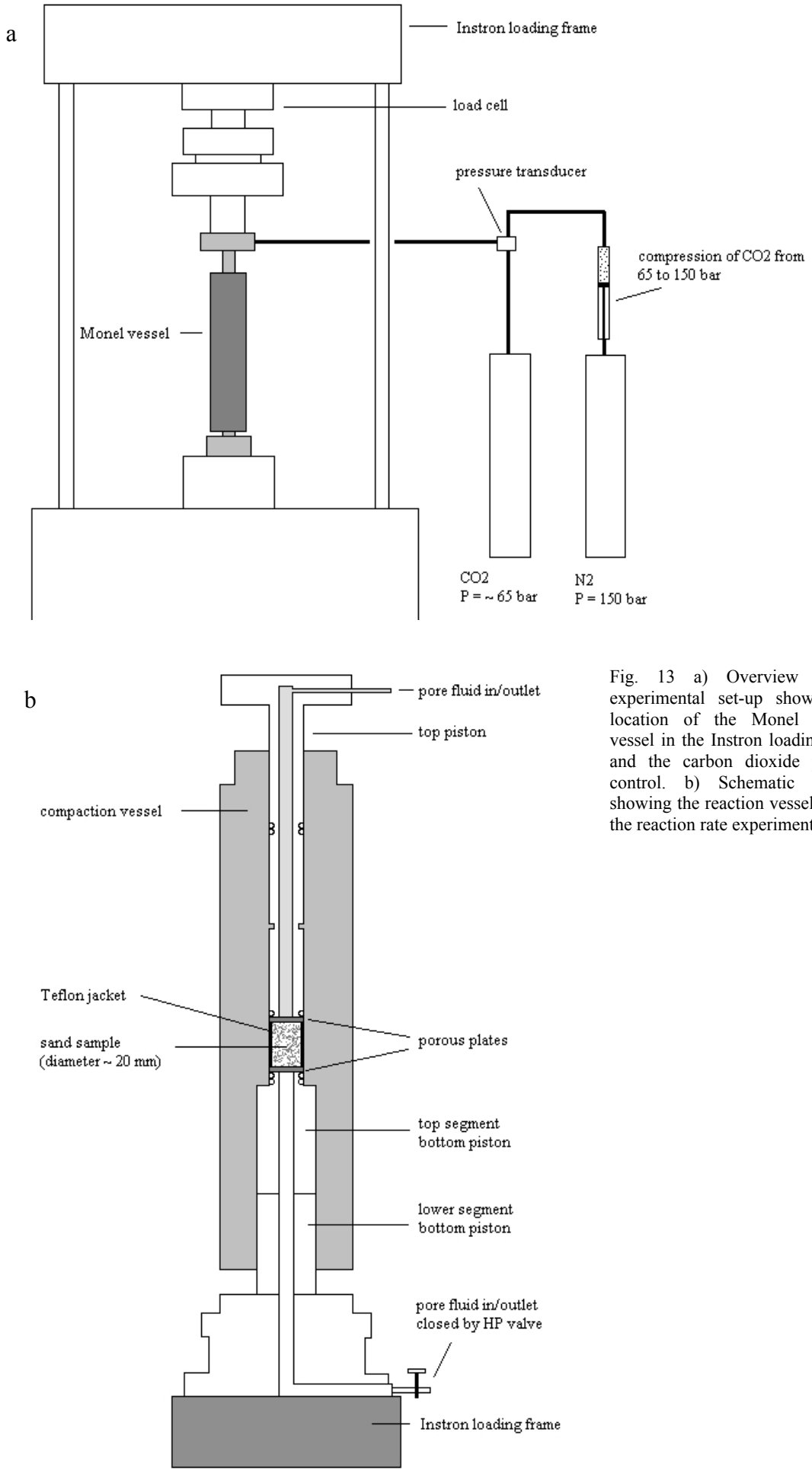

Fig. 13 a) Overview of the experimental set-up showing the location of the Monel reaction vessel in the Instron loading frame and the carbon dioxide pressure control. b) Schematic diagram showing the reaction vessel used in the reaction rate experiments.

effect on the dissolution rate is usually expressed with the Arrhenius equation

$$k_+ = A\exp\left(-\frac{E_a}{RT}\right) \qquad (28)$$

where k_+ is the forward rate constant, A is the pre-experimental factor, E_a is the activation energy, R is 8.3145 J/mol K, and T is the temperature. In general, the activation energy for the dissolution of Na-rich feldspars is on average ~ 70 kJ/mol. Sorai et al. (2005) determined a lower activation energy for the dissolution rate of Ca-rich anorthite, ~ 6 kJ/mol, in CO_2-charged water. Compared to other dissolution rate studies on Ca-rich feldspars this is a rather low value, e.g. ~ 13-26 kJ mol for anorthite (Oelkers & Schott, 1995) and even ~ 71-81 kJ/mol (Suzuki et al., 1996) for labradorite. The value for the activation energy determined by Sorai et al. (2005) is questionable, therefore, it is assumed that the activation energy for the dissolution of anorthite is ~ 18.4 kJ/mol, i.e. the average value determined by Oelkers and Schott (1995). Now, quantifying the effect of temperature, it is seen that the dissolution rate of anorthite is enhanced by ~ 1.5 orders of magnitude when the temperature is raised from room temperature to 100°C, ~ 2.75 orders of magnitude when raised to 200°C, and ~ 3.5 orders of magnitudes when raised to 300°C.

5.1.2 Pressure effect on dissolution rate

The effect of carbon dioxide pressure on the dissolution rate of feldspars, or any other mineral, is less well investigated, and also more difficult to determine since the dissolution of CO_2 in solution, consequently, results in a lowering of the pH. Berg and Banwart (2000) investigated the effect of carbon dioxide, at atmospheric pressure, on the dissolution rate of anorthite. They claimed that the dissolution of anorthite is slightly accelerated by the presence of CO_2, due to the formation of $\equiv Al\text{-}CO_3^-$ surface complexes. On the contrary, other studies (e.g. anorthite and augite, $P_{CO2} = 10^{-3.5}$ - 1 bar (Brady & Carroll, 1994); diopside, forsterite and hornblende, P_{CO2} = 1 bar (Golubev et al., 2005); labradorite, $P_{CO2} = 10^{-3.5}$ – 20 bars (Carroll & Knauss, 2005); calcite, dolomite and magnesite, P_{CO2} = 50 bars (Pokrovsky et al., 2005); anorthite, P_{CO2} = 100 bars (Sorai et al., 2005)) have shown that carbon dioxide pressure has no significant effect on the dissolution rate. They all agreed that any effects observed could be accounted for by the dissolution of CO_2 and the resulting acidity in the water, which accelerated dissolution.

5.1.3 Effect of salinity on dissolution rate

Cations in solution may influence the dissolution rate of quartz and feldspars. Studies have shown that quartz dissolution is significantly enhanced in Na-containing solutions, this due to the formation of Na-surface complexes (Dove & Crerar, 1990; Dove & Elston, 1992; Berger et al., 1994; Dove & Nix, 1997). Both Berger et al. (1994) and Dove and Elston (1992) modelled the effect of sodium ions on the dissolution rate of quartz as a function of pH (Fig. 12). They showed that the addition of 0.2 molar of Na^+ to a solution increases the dissolution rate by approximately one order of magnitude at near-neutral to slightly alkaline pH. However, it should be noted that, they predict that this effect will diminish to almost zero at low pH! The results for quartz are in contrast with those for feldspars. Studies of the effect of NaCl on the dissolution rate of various plagioclase feldspars (Stillings & Brantley, 1995; Blake & Walter, 1999) have shown that salinity significantly decreases the rate of dissolution, at both near-neutral and acid pH. In the presence of 1M of NaCl the dissolution rate of labradorite is reduced by ~50% (Blake & Walter, 1999)! This effect can be explained by surface complexation, in particular competition between Na^+ and H^+ for surface exchange sites. As the concentration of sodium ions in solution increases, the concentration of hydrogen ions reacting with the feldspar surface decreases. Therefore, the decrease in dissolution rate, due to the addition of NaCl, is directly related to the decrease of adsorbed H^+.

5.2 Volumetric reaction vessel

The method used will not be the one that is commonly adopted: solubility experiments, either in a batch or flow-through reactors, with occasional fluid sampling. Instead, a servo-controlled loading machine, or Instron, will be used. A schematic representation of this machine, and its reaction vessel, are shown in Fig. 13. The reaction vessel consists of a free-moving top piston and a fixed bottom

piston, both encapsulated by the compaction vessel, with the sample in between. In "load-control" the loading frame will exert a constant load on the sample. When a load is applied to the sample the top piston will start to move when the sample is being compacted under this load. This movement of the top piston can be accurately logged and tracked through time. Usually the Instron is used for compaction creep experiments, however, for the reaction rate experiments it will be used for a quite different purpose.

A schematic blow-up of the set-up of the reaction vessel, for the reaction rate experiments, is shown in Fig. 14. As can be seen the top piston will not exerts any force on the sample, as is usually the case, it will merely be used to keep the CO_2 pressure in the system constant. This will be done as follows: when reaction occurs in the system carbon dioxide, and water, will be consumed, resulting in a reduction of CO_2 pressure, since the loading frame is set to keep the pressure constant, the top piston will be moved into the vessel to correct the pressure drop. The resulting piston displacement, or volume change, will be monitored accurately and is directly related to the reaction rate of anorthite, or consumption rate of CO_2 and H_2O. For now this relationship can be described as

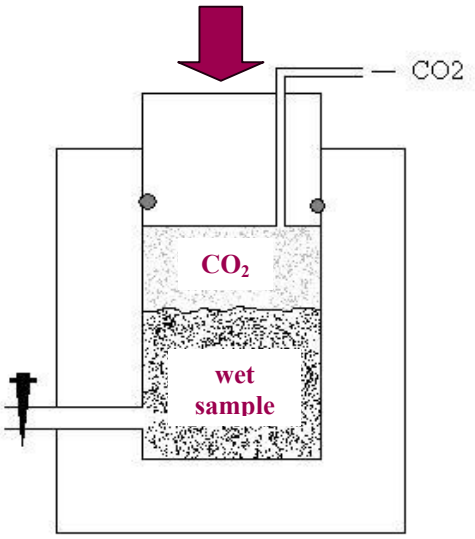

Fig. 14 Schematic blow-up of the reaction vessel, as set-up for reaction rate experiments.

$$R = \frac{\dot{V}}{(A_s C)} \qquad (29)$$

where, R is the reaction rate [mol/m^2 s], $\dot{V}$ is the measured volume change rate with time [m^3/s], A_s is the total surface area of the system [m^2], and C is a constant, as a function of pressure and temperature, which contains the molar volumes of the dissolving and precipitating solids, as well as those of carbon dioxide and water, which are a function of P and T. In a later stage this equation will be expanded to also include the *reactive* surface area of the system, instead of the total surface area, and the change of grain size over time. Predictions, using available kinetic data, showed that under the experimental conditions, i.e. 80°C, P_{CO2} = 100 bars, and 1.2 g of anorthite sample, a total volume change, due to reaction and dissolution of CO_2 into the pore water, was expected of ~ 1cm^3.

Experiments, performed to date, using the Instron to measure the reaction rate proved that the reaction was not only very slow, but that the sensitivity of the apparatus was not sufficient to measure the minor displacements occurring during reaction. A similar system is being developed, which works in a similar manner but achieves much higher accuracy through the use of a very narrow diameter piston driven into the reaction vessel by a servo hydraulic controlled unit.

5.3 Batch experiments

In order to get a general idea of the reaction occurring in the anorthite-CO_2-H_2O system, batch experiments, using a cold-seal pressure vessel, are being set-up. The goal of the experiments is to test the influence of the various parameters, as described above, on the reaction, and to optimise the reaction rate.

The set-up of the experiments is depicted schematically in Fig. 15. The "reaction vessel" consists of a Monel pot, fixed to a stainless steel support rod. The volume of the pot is approximately 1 ml and a screw-on lid, containing a 5µm porous plate, closes it off. The pot and support rod are located into the pressure vessel as shown in Fig. 14. The bomb is filled with carbon dioxide, at a constant pressure, and the whole system will be heated up to a constant temperature. Due to the cooling at the bottom of the bomb, a strong temperature gradient exists throughout the bomb, which may cause water vapour in the bomb to diffuse through the CO_2 to the cooler parts, where it will condense. To prevent this, a PEEK ring is placed between the pot and the rod. When the bomb is heated up the ring will expand and close off, but not seal off the top part of the bomb, preventing the water moving freely down the bomb. The

experiment is terminated by letting of the pressure, before cooling down the system. By letting the pressure off prior to cooling, the water present evaporates and no further reactions will occur, e.g. dissolution of the formed products.

FTIR and SEM analysis of the first experiments are shown in Figures 16 and 17. From the FTIR spectrum it is clear that in the reacted sample a phase has grown which contains water incorporated into its crystal structure, e.g. broad peak around 3400-3500 cm^{-1} and sharp peak at 1616 cm^{-1}. Another interesting peak appears around 1350 cm^{-1}, which could be interpreted as a HCO_3^- bond. Though it is possible to identify minerals by FTIR, the results are not yet conclusive about the composition of the mineral phases formed. In addition to FTIR the samples were analysed by SEM-EDX, of which the results are shown in Fig. 16. Due to the very small grain size of the precipitated phases no good analyses by EDX was possible. However, the pictures indicate the precipitation of a platy mineral, which could very well be a clay mineral, and of more lathe-like crystals of a second mineral.

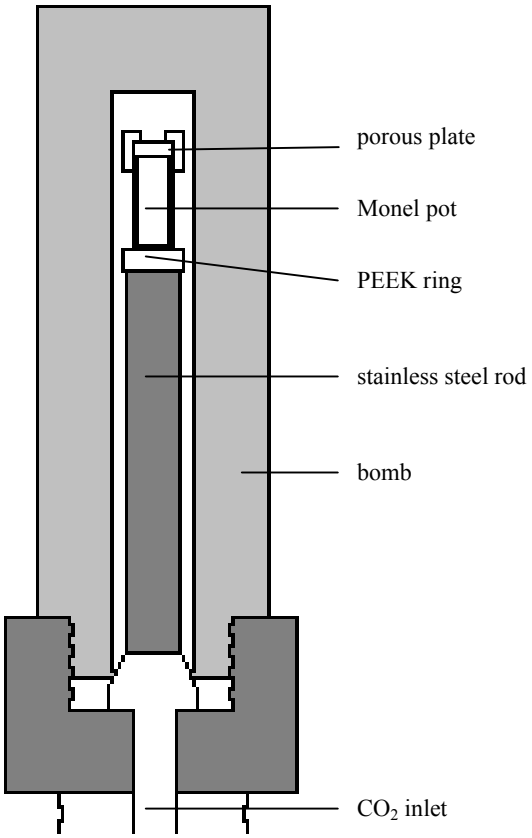

Fig. 15 Schematic diagram showing the set-up of the pressure vessel experiment.

To date few other experimental studies have been done on CO_2 sequestration in reservoir rocks (Shiraki & Dunn, 2000; Kaszuba et al., 2003; Bateman et al., 2005; Kaszuba et al., 2005) as most studies focus on predicting mineral sequestration using computer models (Shiraki & Dunn, 2000; Xu et al., 2004; Bateman et al., 2005; Lagneau et al., 2005; Xu et al., 2005). An exception is seen in the experiments of Kaszuba et al. (2003; 2005), who studied a model aquifer-aquitard system reacting with brine and supercritical carbon dioxide. The system contained minerals like quartz, feldspars, i.e. oligoclase and microcline, micas, i.e. biotite, and clays, i.e. illite. At a temperature of 200°C and a CO_2 pressure of 200 bars they observed the growth of smectite clay minerals on oligoclase and biotite, small magnesite rosettes coating biotite, precipitation of larger magnesite crystals, and precipitation of analcime, which in turn was coated with kaolinite, smectite and biotite. Though, their experiments show that CO_2 mineralisation is possible, they did not derive any reaction rates for the occurring reactions.

5.4 FTIR spectroscopy

In the PT-range of interest only limited measurements of the solubility of CO_2 in water and brine have been made. We are now using a relatively unexplored method to improve the data density inside this range, as well as outside. By using a Fourier Transform Infrared Microscope (FTIR), in combination with a specially built high pressure-temperature cell, it is possible to measure, very accurately, the concentration of aqueous carbon dioxide in solution. In addition, it has also proven to be a good method for quantifying the dissolution rate of gaseous CO_2 into solution, forming aqueous CO_2.

Table 6 Infrared absorption frequencies of CO_2 and H_2O	
antisymmetrical stretching, $CO_{2(g)}$	2349 cm^{-1}
antisymmetrical stretching, $CO_{2(aq)}$	2342 cm^{-1}
stretching, H_2O	3404.0 cm^{-1}
bending, H_2O	1643.5 cm^{-1}

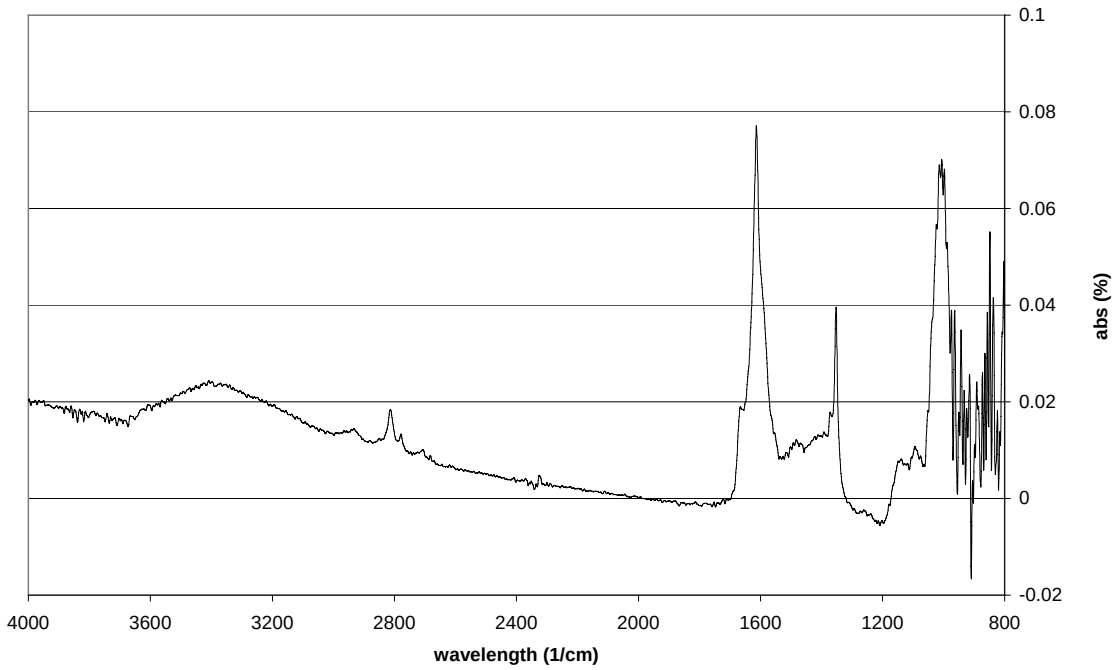

Fig. 16 FTIR spectrum of a sample from the pressure vessel experiment. Reaction took place at 300°C and P_{CO2} = 60 bars for 3 weeks. Clearly visible are the broad peak at 3400-3500 cm^{-1}, and the sharp peak at 1616 cm^{-1}, indicative for a mineral which has water incorporated into its crystal structure, e.g. clay minerals. The peak at 1353 cm^{-1} could be from HCO_3^- bonds. The spectrum for anorthite is visible at wavelengths from 1130cm^{-1} and lower.

The wavenumbers, at which the various carbon dioxide peaks (Jones & McLaren, 1958; Falk & Miller, 1992) and water peaks (Venyaminov & Prendergast, 1997) can be observed, are accurately known (Table 6). From the ratio between the peak absorbence of $CO_{2(aq)}$ and H_2O, the concentration of aqueous carbon dioxide in solution can be calculated using Lambert-Beer's law

$$\frac{A_{CO_2}}{A_{H_2O}} = \frac{\varepsilon_{CO_2}}{\varepsilon_{H_2O}} \frac{c_{CO_2}}{c_{H_2O}} \tag{30a}$$

where A_i is the peak absorbance of species i, ε_i is the peak molar absorptivity of species i, and c_i is the concentration of species i in the mixture in mol/cm^3. By expressing the concentration of CO_2 in solution as a ratio of the peak absorbence of carbon dioxide and water knowing the path length is no longer necessary. Since concentration is defined as the number of moles of species i in the mixture, the ratio between the concentration of carbon dioxide and water, in solution, can also be expressed as N_{CO2}/N_{H2O}, with N is the number of moles of species i. Now the ratio between the peak absorbence of both species can be expressed as a function of CO_2 solubility, m_{CO2} [mol CO_2/kg water]

$$\frac{A_{CO_2}}{A_{H_2O}} = 18.02 \cdot 10^{-3} m_{CO_2} \frac{\varepsilon_{CO_2}}{\varepsilon_{H_2O}} \tag{30b}$$

Hence, FTIR can be used as a method for measuring m_{CO2} if the peak molar absorptivities of the various species in solution are known. Fig. 18 shows the first results of FTIR measurements on the solubility of carbon dioxide in pure water. The measuring cell was pre-pressurised with 23 bars of CO_2 pressure, and measurements were started, directly after the pressure was increased to 40 bars. The change of the $CO_{2(aq)}$ peak height with time is shown in Fig. 18. It can be seen that the peak, and hence the concentration of CO_2 in solution, is increasing rapidly during the first 15 min after pressurisation. The very rapid dissolution of carbon dioxide in water, within one hour, is in agreement with the observations of Markham and Kobe (1941) and Todheide and Franck (1963). This is in contrast with the general assumption that carbon dioxide dissolution requires up to 24 hours before equilibrium is established (Harned & Davis, 1943; Takenouchi & Kennedy, 1965b; Nighswander et al., 1989; Czernichowski-Lauriol et al., 1996; Teng et al., 1997; Bando et al., 2003; Portier & Rochelle, 2005).

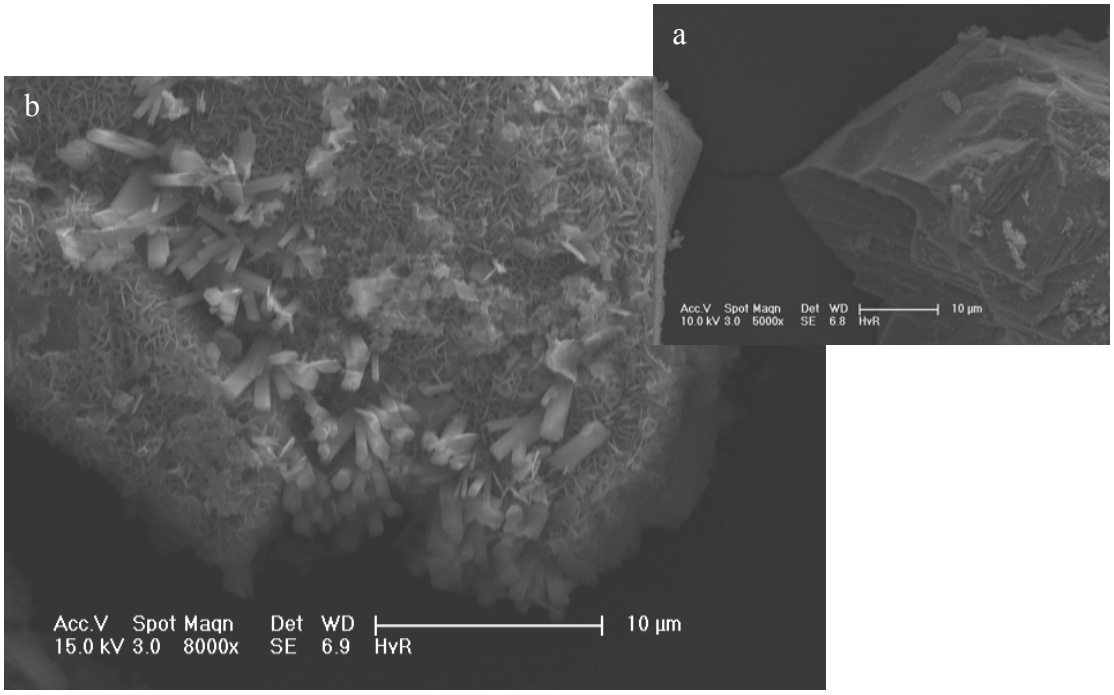

Fig. 17 SEM-EDX analyses of pressure vessel experiments. a) unreacted anorthite; b) after reaction at 300°C and P_{CO2} = 60 bars, for 1 week. Clearly visible is the growth of a platy mineral, grain size less than 1 µm, which give the anorthite a fussy appearance, and a larger, stick-like mineral, ~ 2 µm.

In addition to measuring the solubility and dissolution rate of CO_2 in solution, FTIR will also be used shortly to measure the reaction rate of the feldspar-CO_2-H_2O system. Measurements have already shown that the peak area, of the characteristic peaks for a mineral, can directly be correlated to concentration. By monitoring the concentration of the various absorbing species in solution, it will be possible to calculate the reaction rate, as function of temperature and pressure. However, determining the reaction rate as a function of grain size will be limited to grain sizes of a few microns, as absorbence is related to path length and will reach a maximum when the path length is too large. The

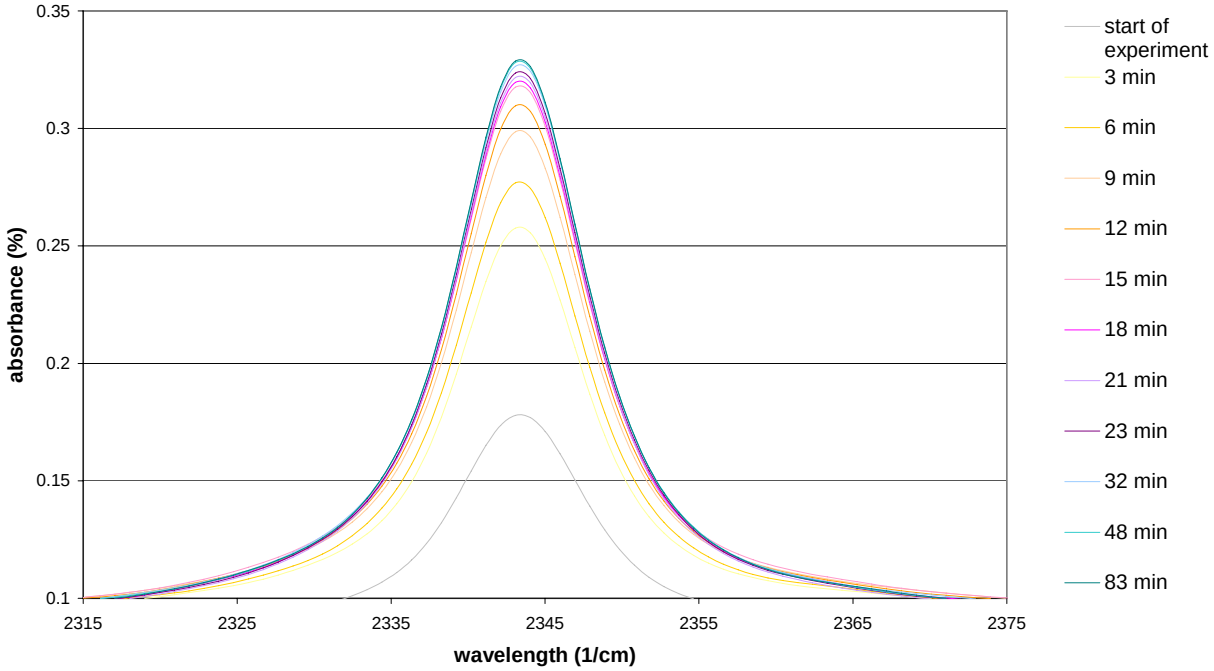

Fig. 18 FTIR spectra of the $CO_{2(aq)}$ peak as a function of time. At the start of the experiment the carbon dioxide pressure is 23 bars, and it is raised to 40 bars. The graphs show the evolution of the dissolution of CO_2 in water at room temperature.

first results of this experiment are shown in Figure 19. The water peaks, which were visible in the sample from the pressure vessel, are now overprinted by the aqueous solution. However, the bicarbonate peak is still visible, which could indicate that in both experiments similar reaction products are formed. More experiments are needed to investigate the nature of this precipitate.

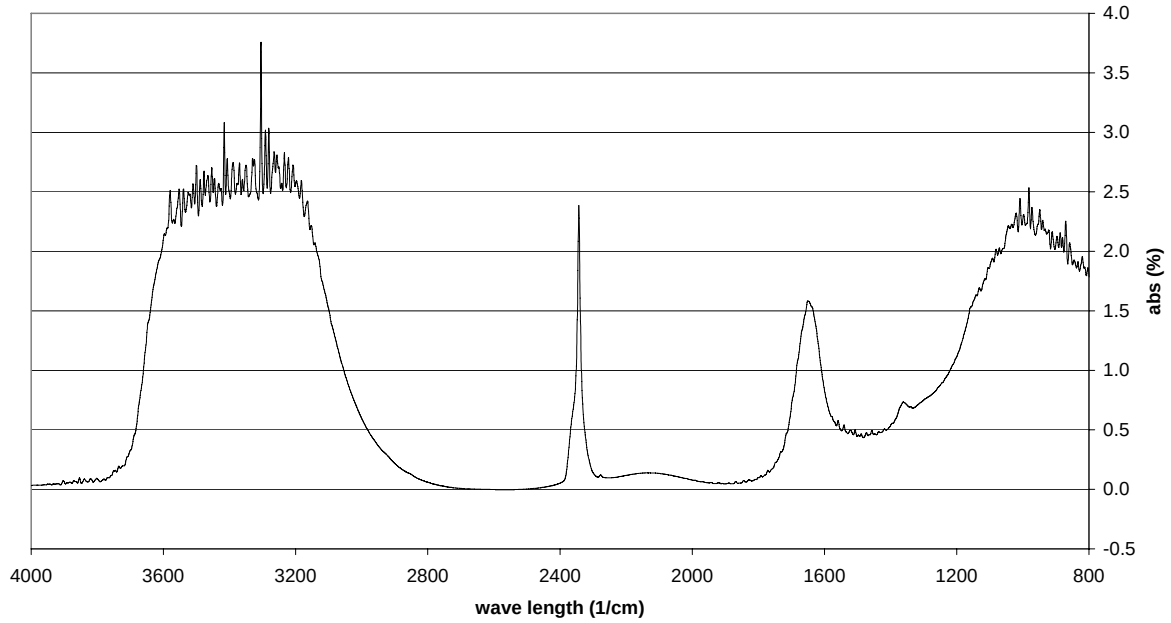

Fig. 19 FTIR spectrum of reacting anorthite at room temperature and 100 bars CO_2 pressure, after 10 days. When comparing this spectrum to that of the pressure vessel (Fig. 15) the bicarbonate peak is visible in both spectra at 1353 cm^{-1}, which may be an indication that in both experiment the same products are formed. The water peaks in the latter are overprinted in this spectrum due to the presence of an aqueous solution. The dissolved CO2, $CO_{2(aq)}$, peak is seen at 2342 cm^{-1}.

5.5 Atomic Force Microscopy

A last method to get additional information on the dissolution rate of feldspar in aqueous solutions containing supercritical carbon dioxide is by measuring the surface retreat of crystals as a function of time, using atomic force microscopy. Imaging of feldspar surfaces by AFM has already been done on albite (Hochella Jr. et al., 1990; Drake & Hellmann, 1991), labradorite (Jordan et al., 1999) and anorthite (Jordan et al., 1999; Lüttge et al., 1999; Sorai et al., 2005). However, Sorai et al. (2005) is the only one that used this technique to determine the dissolution rate of feldspar. Lüttge et al. (1999) also used surface retreat to quantify anorthite dissolution rates; only they measured the observed vertical movements by vertical scanning white light interferometry (VSWLI).

In individual experiments the dissolution rate of anorthite, bytownite, and labradorite, in aqueous solutions containing supercritical CO_2, will be determined. Samples will consist of cleaved crystals, preferably showing all of the main crystal surfaces, i.e. (100), (010), and (001). In order to be able to quantify the surface retreat it is necessary to create a reference surface by sealing off part of the crystal to the reacting solution. An unreacted surface can be obtained by, for example, Au-sputtering on the surface (Sorai et al., 2005) or covering the surface with silicon rubber (Lüttge et al., 1999). Important, though, is that the masking material can easily be removed without leaving residue on the reference surface. The samples will be submerged in solution, charged with carbon dioxide at a constant pressure, for a given period of time. After reaction the surface retreat will be measured, relatively to the reference surface. Dissolution rates can be determined from the proceeding surface retreat with time, and, since crystals with several different crystal surfaces were used, as a function of crystallographic orientation. So far, we have mainly been concentrating on setting up the AFM and acquiring suitable feldspar crystals. An example of a surface scan from an, unreacted, anorthite crystal is shown in Fig. 20. It can be seen that height differences on the nanometer scale can be resolved by AFM.

As mentioned, the literature on measuring the dissolution rate of crystals by surface retreat is not extensive. Both Sorai et al. (2005) and Lüttge et al. (1999) measured the dissolution rate of anorthite on

the cleavage planes. However, their results differed by one order of magnitude at a pH of 3 and 25°C, $6 \cdot 10^{-10}$ mol/m^2 s (Sorai et al., 2005) compared to $5.7 \cdot 10^{-9}$ mol/m^2 s (Lüttge et al., 1999). A study on the effect of crystallographic orientation on dissolution rate of labradorite (Suzuki et al., 1996) has shown that dissolution on the plane normal to cleavage, i.e. (100), is slightly faster than on the cleavage planes themselves, i.e. (010) and (001). This seems to be due to the higher etch pit density on (100), as a result of (010) and (001) cleavage. As etch pits are locations of weakness in the crystal structure, it was concluded that the microtexture, e.g. cleavage and twinning, plays a larger role on controlling dissolution rates than crystallographic orientation. This experiment can shed more light on the dependence of dissolution rate on crystallographic orientation.

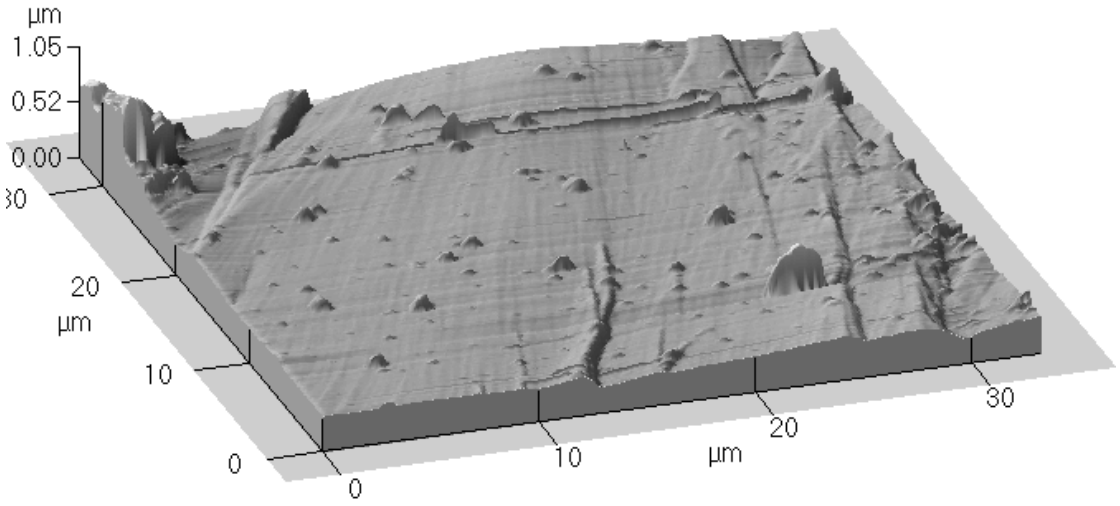

Fig. 20 AFM scan of the surface of an anorthite grain. As can be seen AFM can resolve height differences on the nanometer scale.

6. Conclusions

In addition to the thermodynamic and kinetic data of the relevant minerals, it is also important to be able to predict the behaviour of the water-CO_2±salts system, as well as the solubility of carbon dioxide in aqueous solution. A review of the Equations of State, available in the literature, for the pure end-members systems as well as the water-CO_2 mixture has been made. Relevant EOS have been described in the appendices, and a CO_2-solubility model, which covers the PT-conditions of interest, has been taken from the literature. The main findings are

- The thermodynamic properties of carbon dioxide are best described by the Equation of State by Duan et al. (1992a). Their EOS covers the temperature range from 0 to 1000°C and the pressure range from 0 to 8000 bars.
- The EOS released by The International Association for the properties of Water and Steam (IAPWS) (Wagner et al., 2000) best describes the thermodynamic properties of water. The IAPWS-97 covers temperatures from 0 to 800°C up to pressures of 1000 bars, and temperatures from 800 to 2000°C up to 100 bars.
- The thermodynamic behaviour of the CO_2-H_2O system is best described by the EOS developed by Duan et al. (1992b). The pressure-temperature range for applying this EOS is from 50 to 1000°C and 0 to 1000 bars.
- The solubility of CO_2 in aqueous solution is best modelled with the solubility model derived by Duan and Sun (2003; 2005). On average the error of the model, compared to experimental data, is less than 7%), though at higher pressures the error increases to up to 30%.

The effects of temperature, pressure, and salinity on the solubility of carbon dioxide can be summarised as follows

- The solubility of CO_2 in solution decreases with increasing temperature, at temperatures below 100°C, at constant pressure and salinity. When the temperature is above this value the solubility increases again with temperature.
- With increasing pressure, at constant temperature and salinity, the solubility of CO_2 in solution increases. This pressure effect diminishes with increasing pressure, so at lower pressures the solubility increases more rapidly than at higher pressures, as a function of pressure.
- The addition of salt to solution leads to the decrease of carbon dioxide solubility. The magnitude of this effect is determined by the composition of the salt; monovalent salt solutions, e.g. NaCl or KCl, inhibit CO_2 dissolution more than divalent salt solutions, e.g. $CaCl_2$ or $MgCl_2$.

Though the data available in the literature is not always complete and does not cover our in-situ conditions, preliminary equations have been derived that can be used for estimating the extent and rate of CO_2 sequestration. The maximum, and minimum, amount of carbonate that can precipitate in one cubic meter of anorthite-rich sandstone rock per second is given by:

$$\dot{M}_{\max} = 60\left(\frac{X\,\mathrm{R}(P_{CO_2},T)\,m_{\text{calcite}}}{d(t)}\right) \qquad [\text{kg/m}^3\text{s}]$$

$$\dot{M}_{\min} = 60\left(\frac{X\,\mathrm{R}(P_{CO_2},T)\,m_{\text{calcite}}}{d(t)}\right)\left(1-\frac{1-2\varphi}{N}\right) \qquad [\text{kg/m}^3\text{s}]$$

And, the maximum amount of carbonate that can precipitate, as a function of either the anorthite or water content is given by:

$$M_{\text{T,anorthite}} = \mathrm{N}^{\text{moles}}_{\text{anorthite}} m_{\text{calcite}} = \frac{10\,\rho_{\text{anorthite}}\,m_{\text{calcite}}\,X}{m_{\text{anorthite}}} \qquad [\text{kg/m}^3]$$

$$M_{\text{T,H}_2\text{O}} = 0.5\,\mathrm{N}^{\text{moles}}_{\text{water}} m_{\text{calcite}} = \frac{5\,\rho_{\text{H}_2\text{O}}\,m_{\text{calcite}}\,W}{m_{\text{H}_2\text{O}}} \qquad [\text{kg/m}^3]$$

Precipitation of both carbonates and clays will influence the porosity and permeability of the sandstone reservoir. The extent of this depends on the mechanism of feldspar dissolution and the location of precipitation. In the most extreme case the reservoir will be completely clogged up, in the other the reservoir will remain porous and permeable to fluids. The former is unlikely to be a good representation of the actual process occurring in a reservoir after CO_2 injection. It is more likely that the reservoir remains permeable to fluids to some extent.

Feldspar dissolution rates have proven to be very slow. Studies have shown that temperature can increase the dissolution rate by several orders of magnitude, when on the other hand carbon dioxide pressure does not seem to have any effect. Salinity even decreases the dissolution rate of feldspars. Several experimental set-ups have been tested and have shown promising results. Experiments have proven that reaction of CO_2 with feldspar leads to the precipitation of secondary phases. The exact composition of these phases is still unclear, though different experimental set-ups, at different PT-conditions, gave similar results. Since the results look promising work will continue along these paths.

Acknowledgements

I would like to thank Peter van Krieken and Gert Kastelein for their technical support in the lab. Also, I would also to thank Prof. Dr. Chris Spiers for his useful discussions, and comments on my work. Last but not least, I would like to thank Leslie Kramers for his excellent work on determining the solubility of CO_2 in aqueous solution. His results are of significant importance to this research.

References

Amrhein, C. and D. L. Suarez, 1992, Some factors affecting the dissolution kinetics of anorthite at 25°C, *Geochim. Cosmochim. Acta, 56*, 1815-1826.

Bachu, S., W. D. Gunter and E. H. Perkins, 1996, Chapter 3: Carbon dioxide disposal, *Aquifer disposal of carbon dioxide: hydrodynamic and mineral trapping - proof of concept,* 11-22.

Bando, S., F. Takemura, M. Nishio, E. Hihara and M. Akai, 2003, Solubility of CO_2 in aqueous solutions of NaCl at 30 to 60°C and 10 to 20 MPa, *J. Chem. Eng. Data, 48*, 576-579.

Bateman, K., A. M. Turner, J. Pearce, D. J. Noy, D. Birchall and C. Rochelle, 2005, Large-scale column experiment: study of CO_2, porewater, rock reactions and model test case, *Oil and Gas Sci. Tech., 60, #1*, 161-175.

Bauer, A. and G. Berger, 1998, Kaolinite and smectite dissolution rate in high molar KOH solutions at 35° and 80°C, *Appl. Geochem., 13, # 7*, 905-916.

Berg, A. and S. A. Banwart, 2000, Carbon dioxide mediated dissolution of Ca-feldspar: implications for silicate weathering, *Chem. Geol., 163*, 25-42.

Berger, G., E. Cadore, J. Schott and P. Dove, 1994, Dissolution rate of quartz in lead and sodium electrolyte solutions between 25 and 300°C: effect of the nature of surface complexes and reaction affinity, *Geochim. Cosmochim. Acta, 58, #2*, 541-551.

Blake, R. E. and L. M. Walter, 1999, Kinetics of feldspar and quartz dissolution at 70-80 C and near-neutral pH: effects of organic acids and NaCl, *Geochim. Cosmochim. Acta, 63, #13-14*, 2043-2059.

Blum, A. and A. Lasaga, 1988, Role of surface speciation in the low-temperature dissolution of minerals, *Nature, 331*, 431-433.

Bowers, T. S. and H. C. Helgeson, 1983, Calculation of the thermodynamic and geochemical consequences of nonideal mixing in the system H_2O-CO_2-NaCl on phase relations in geologic systems: equation of state for H_2O-CO_2-NaCl fluids at high pressures and temperatures, *Geochim. Cosmochim. Acta, 47*, 1247-1275.

Brady, P. V. and S. A. Carroll, 1994, Direct effects of CO_2 and temperature on silicate weathering: possible implications for climate control, *Geochim. Cosmochim. Acta, 58, # 8*, 1853-1856.

Cama, J., J. Ganor, C. Ayora and C. A. Lasaga, 2000, Smectite dissolution kinetics at 80°C and pH 8.8, *Geochim. Cosmochim. Acta, 64, # 15*, 2701-2717.

Carroll, J. J., J. D. Slupsky and A. E. Mather, 1991, The solubility of carbon dioxide in water at low pressure, *J. Phys. Chem. Ref. Data, 20, # 6*, 1201-1209.

Carroll, S. A. and K. G. Knauss, 2005, Dependence of labradorite dissolution kinetics on $CO_{2(aq)}$, $Al_{(aq)}$, and temperature, *Chem. Geol., 217*, 213-225.

Casey, W. H., H. R. Westrich and G. R. Holdren, 1991, Dissolution rates of plagioclase at pH = 2 and 3, *Am. Mineral., 76*, 211-217.

Czernichowski-Lauriol, I., B. Sanjuan, C. Rochelle, K. Bateman, J. Pearce and P. Blackwell, 1996, Chapter 7: Inorganic geochemistry, *The underground disposal of carbon dioxide, JOU2 CT92-0031,* 183-276.

Devidal, J.-L., J. Schott and J.-L. Dandurand, 1997, An experimental study of kaolinite dissolution and precipitation kinetics as a function of chemical affinity and solution composition at 150°C, 40 bars, and pH 2, 6.8, and 7.8, *Geochim. Cosmochim. Acta, 61, # 24*, 5165-5186.

Dove, P. M. and D. A. Crerar, 1990, Kinetics of quartz dissolution in electrolyte solutions using a hydrothermal mixed flow reactor, *Geochim. Cosmochim. Acta, 54*, 955-969.

Dove, P. M. and S. F. Elston, 1992, Dissolution kinetics of quartz in sodium chloride solutions: analysis of existing data and a rate model for 25°C, *Geochim. Cosmochim. Acta, 56*, 4147-4156.

Dove, P. M. and C. J. Nix, 1997, The influence of the alkaline earth cations, magnesium, calcium, and barium on the dissolution kinetics of quartz, *Geochim. Cosmochim. Acta, 61, # 16*, 3329-3340.

Drake, B. and R. Hellmann, 1991, Atomic forcing microscopy imaging of the albite (010) surface, *Am. Mineral., 76*, 1773-1776.

Duan, Z. and J. Hu, 2004, A new cubic equation of state and its applications to the modelling of vapor-liquid equilibria and volumetric properties of natural fluids, *Geochim. Cosmochim. Acta, 68, 14*, 2997-3009.

Duan, Z., N. Møller and J. H. Weare, 1992a, An equation of state for the CH_4-CO_2-H_2O system: I pure systems from 0 to 1000°C and 0 to 8000 bar, *Geochim. Cosmochim. Acta, 56*, 2605-2617.

Duan, Z., N. Møller and J. H. Weare, 1992b, An equation of state for the CH_4-CO_2-H_2O system: II mixtures from 50 to 1000°C and 0 to 1000 bar, *Geochim. Cosmochim. Acta, 56*, 2619-2631.

Duan, Z., N. Møller and J. H. Weare, 1995, Equation of state for the NaCl-H_2O-CO_2 system: prediction of phase equilibria and volumetric properties, *Geochim. Cosmochim. Acta, 59, # 14*, 2869-2882.

Duan, Z., N. Møller and J. H. Weare, 1996, A general equation of state for supercritical fluid mixtures and molecular dynamics simulation of mixture PVTX properties, *Geochim. Cosmochim. Acta, 60, 7*, 1209-1216.

Duan, Z. and R. Sun, 2003, An improved model calculating CO_2 solubility in pure water and aqueous NaCl solutions from 273 to 533 K and from 0 to 2000 bar, *Chem. Geol., 193*, 257-271.

Duan, Z., R. Sun, C. Zhu and I.-M. Chou, 2005, An improved model for the calculation of CO_2 solubility in aqueous solutions containing Na^+, K^+, Ca^{2+}, Mg^{2+}, Cl^-, and SO_4^{2-}, *Marine Chem., in press*.

Ellis, A. J. and R. M. Golding, 1963, The solubility of carbon dioxide above 100°C in water and in sodium chloride solutions, *Am. J. Sci., 261*, 47-60.

Falk, M. and A. G. Miller, 1992, Infrared spectrum of carbon dioxide in aqueous solution, *Vib. Spectr., 4*, 105-108.

Fisher, J. R., 1976, The volumetric properties of H_2O - a graphical portrayal, *J. Res. USGS, 4, # 2*, 189-193.

Ganor, J., J. L. Mogollón and A. C. Lasaga, 1995, The effect of pH on kaolinite dissolution rates and activation energy, *Geochim. Cosmochim. Acta, 59, # 6*, 1037-1052.

Golubev, S. V., O. S. Pokrovsky and J. Schott, 2005, Experimental determination of the effect of dissolved CO_2 on the dissolution kinetics of Mg and Ca silicates at 25°C, *Chem. Geol., 217*, 227-238.

Guéguen, Y. and V. Palciauskas, 1994, Introduction to the physics of rocks, *Princeton University Press*, 294 p.

Hamilton, J. P., S. L. Brantley, C. G. Pantano, L. J. Criscenti and J. D. Kubicki, 2001, Dissolution of nepheline, jadeite and albite glasses: toward better models for aluminosilicate dissolution, *Geochim. Cosmochim. Acta, 65, # 21*, 3683-3702.

Hangx, S. J. T., 2005, Subsurface mineralisation: Rate of CO_2 mineralisation and geomechanical effects on host and seal formations - a review of relevant reactions and reaction rate data, *WP 4.1-2-05*, 63 p.

Harned, H. S. and R. Davis, 1943, The ionization constant of carbonic acid in water and the solubility of carbon dioxde in water and aqueous salt solutions from 0 to 50°, *J. Am. Chem. Soc., 65*, 2030-2037.

Hellmann, R., 1994, The albite-water system: part I The kinetics of dissolution as a function of pH at 100, 200, and 300°C, *Geochim. Cosmochim. Acta, 58, # 2*, 595-611.

Hochella Jr., M. F., C. M. Eggleston, V. B. Elings and M. S. Thompson, 1990, Atomic structure and morphology of the albite {010} surface: an atomic-force miscroscope and electron diffraction study, *Am. Mineral., 75*, 723-730.

Holloway, S., 1996, Chapter 2: Background, *The underground disposal of carbon dioxide, JOU2 CT92-0031,* 3-5.

Huertas, F. J., E. Caballero, C. Jiménez de Cisneros, F. Huertas and J. Linares, 2001, Kinetics of montmorillonite dissolution in granitic solutions, *Appl. Geochem., 16*, 397-407.

Jones, L. H. and E. McLaren, 1958, Infrared absorption spectra of SO_2 and CO_2 in aquoeus solution, *J. Chem. Phys., 28*, 995.

Jordan, G., S. R. Higgins, C. M. Eggleston, S. M. Swapp, D. E. Janney and K. G. Knauss, 1999, Acidic dissolution of plagioclase: in-situ observations by hydrothermal atomic force microscopy, *Geochim. Cosmochim. Acta, 63, #19-20*, 3183-3191.

Kaszuba, J. P., D. R. Janecky and M. G. Snow, 2003, Carbon dioxide reaction processes in a model brine aquifer at 200°C and 200 bars: implications for geologic sequestration of carbon, *Appl. Geochem., 18*, 1065-1080.

Kaszuba, J. P., D. R. Janecky and M. G. Snow, 2005, Experimental evaluation of mixed fluid reactions between supercritical carbon dioxide and NaCl brine: relevance to the integrity of a geologic carbon repository, *Chem. Geol., 217*, 277-293.

Kerrick, D. M. and G. K. Jacobs, 1981, A modified Redlich-Kwong equation for H_2O, CO_2, and H_2O-CO_2 mixtures at elevated pressures and temperatures, *Am. J. Sci., 281*, 735-767.

Kiepe, J., S. Horstmann, K. Fischer and J. Gmehling, 2002, Experimental determnation and predictions of gas solubility data for CO_2 + H_2O mixtures containing NaCl or KCl at temperatures between 313 and 393K and pressures up to 10 MPa, *Ind. Eng. Chem. Res., 41*, 4393-4398.

King, M. B., A. Mubarak, J. D. Kim and T. R. Bott, 1992, The mutual solubilities of water with supercritical and liquid carbon dioxide, *J. Supercrit. Fluids, 5*, 296-302.

Knauss, K. G. and T. J. Wolery, 1986, Dependence of albite dissolution kinetics on pH and time at 25°C and 70°C, *Geochim. Cosmochim. Acta, 50*, 2481-2497.
Köhler, S. J., F. Dufaud and E. H. Oelkers, 2003, An experimental study of illite dissolution kinetics as a function of pH from 1.4 to 12.4 and temperature from 5° to 50°C, *Geochim. Cosmochim. Acta, 67, # 19*, 3583-3594.
Lagneau, V., A. Pipart and H. Catalette, 2005, Reactive transport modelling of CO_2 sequestration in deep saline aquifers, *Oil and Gas Sci. Tech., 60, # 2*, 231-247.
Lee, B. I. and M. G. Kesler, 1975, A generalized thermodynamic correlation based on three-parameter corresponding states, *AlChE, 21, #3*, 510-527.
Lide, D. R. (ed.), 2004, CRC Handbook of Physics and Chemistry 85th edition, *Section 6: Fluid properties*, 2656 p.
Lüttge, A., E. W. Bolton and A. Lasaga, 1999, An interferometric study of the dissolution kinetics of anorthite: the role of reactive surface area, *Am. J. Sci., 299*, 652-678.
Malinin, S. D., 1959, The system water-carbon dioxide at high temperatures and pressures, *Geochem. Int., 3*, 292-306.
Malinin, S. D. and N. A. Kurovskaya, 1975, Solubility of CO_2 in chloride solutions at elevated temperatures and CO_2 pressures, *Geochem. Int., 12*, 199-201.
Malinin, S. D. and N. I. Savalyeva, 1972, The solubility of CO_2 in NaCl and $CaCl_2$ solutions at 25, 50, and 75° under elevated CO_2 pressures, *Geochem. Int., 9*, 410-418.
Markham, A. E. and K. A. Kobe, 1941, The solubility of carbon dioxide and nitrous oxide in aqueous salt solutions, *J. Am. Chem. Soc., 63*, 449-454.
Nagy, K. L. and A. C. Lasaga, 1992, Dissolution and precipitation kinetics of gibbsite at 80°C and pH 3: the dependence on solution saturation state, *Geochim. Cosmochim. Acta, 56*, 3093-3111.
Nagy, K. L. and A. C. Lasaga, 1993, Simultaneous precipitation kinetics of kaolinite and gibbsite at 80°C and pH 3, *Geochim. Cosmochim. Acta, 57*, 4329-4335.
Ng, H.-J. and D. B. Robinson, 1985, Hydrate formation in systems containing methane, ethane, propane, carbon dioxide or hydrogen sulfide in the presence of methanol, *Fluid Phase Eq., 21*, 145-155.
Nieva, D. and R. M. Barragán, 2003, HCO-TERNARY: A Fortran code for calculating P-V-T-X properties and liquid vapour equilibria of fluids in the system H_2O-CO_2-CH_4, *Comp. Geosci., 29*, 469-485.
Nighswander, J. A., N. Kalogerakis and A. K. Mehrotra, 1989, Solubilities of carbon dioxide in water and 1 wt% NaCl solution at pressures up to 10 MPa and temperatures from 80 to 200°C, *J. Chem. Eng. Data, 34*, 355-360.
Oelkers, E. H. and J. Schott, 1995, Experimental study of anorthite dissolution and the relative mechanism of feldspar hydrolysis, *Geochim. Cosmochim. Acta, 59, #24*, 5039-5053.
Oxburgh, R., J. I. Drever and Y.-T. Sun, 1994, Mechanism of plagioclase dissolution in acid solution at 25°C, *Geochim. Cosmochim. Acta, 58, # 2*, 661-669.
Peng, D.-Y. and D. B. Robinson, 1976, A new two-constant equation of state, *Ind. Eng. Chem. Fundam., 15, #1*, 59-64.
Pokrovsky, O. S., S. V. Golubev and J. Schott, 2005, Dissolution kinetics of calcite, dolomite, and magnesite at 25°C and 0 to 50 atm pCO_2, *Chem. Geol., 217, #3-4*, 239-255.
Portier, S. and C. Rochelle, 2005, Modelling CO_2 solubility in pure water and NaCl-type water from 0 to 300°C and from 1 to 300 bar: applications to the Utsira Formation at Sleipner, *Chem. Geol., 217, #3-4*, 187-199.
Prutton, C. F. and R. L. Savage, 1945, The solubility of carbon dioxide in calcium chloride-water solutions at 75, 100, 120° and high pressures, *J. Am. Chem. Soc., 67*, 1550-1554.
Redlich, O. and J. N. S. Kwong, 1949, On the thermodynamics of solutions V: an equation of state, fugacities of gaseous solutions, *Chem. Rev., 44*, 233-244.
Seitz, J. C. and J. G. Blencoe, 1999, The CO_2-H_2O system I: experimental dtermination of volumetric properties at 400°C, 10-100 MPa, *Geochim. Cosmochim. Acta, 63*, 1559-1569.
Shiraki, R. and S. L. Brantley, 1995, Kinetics of near-equilibrium calcite precipitation at 100°C: an evaluation of elementary reaction-based and affinity-based rate laws, *Geochim. Cosmochim. Acta, 59, # 8*, 1457-1471.
Shiraki, R. and T. L. Dunn, 2000, Experimental study on water-rock interactions during CO_2 flooding in the tensleep Formation, Wyoming, USA, *Appl. Geochem., 15*, 265-279.
Shmulovich, K. I., V. M. Shmonov, V. A. Mazur and A. G. Kalinichev, 1980, P-V-T and activity concentration relations in the H_2O-CO_2 system (homogeneous solutions), *Geochem. Int., 12*, 1807-1824.

Sorai, M., T. Ohsumi and M. Ishikawa, 2005, Nanoscale surface observation of feldspar dissolved under supercritical CO_2-water-mineral system, *Energy, 30*, 2334-2343.
Span, R. and W. Wagner, 1996, A new equation of state for carbon dioxide covering the fluid region from the triple-point temperature to 1100K at pressures up to 800 MPa, *J. Phys. Chem. Ref. Data, 25, # 6*, 1509-1596.
Stewart, P. B. and P. Munjal, 1970, Solubility of carbon dioxide in pure water, synthetic sea water, and synthetic sea water concentrates at -5° to 25°C and 10- to 45-atm pressure, *J. Chem. Eng. Data, 15, 1*, 67-71.
Stillings, L. L. and S. L. Brantley, 1995, Feldspar dissolution at 25°C and pH 3: reaction stoichiometry and the effect of cations, *Geochim. Cosmochim. Acta, 59, # 8*, 1483-1496.
Suzuki, M., T. Tokuhei, T. Hoshi and K. Tsukimura, 1996, Dissolution process and rate in feldspar: effects of crystallographic orientation, *Mineral. J., 18, #2*, 43-53.
Takenouchi, S. and G. C. Kennedy, 1964, The binary system H_2O-CO_2 at high temperatures and pressures, *Am. J. Sci., 262*, 1055-1074.
Takenouchi, S. and G. C. Kennedy, 1965a, Dissociation pressures of the phase CO_2-5¾H_2O, *J. Geol., 73*, 383-390.
Takenouchi, S. and G. C. Kennedy, 1965b, The solubility of carbon dioxide in NaCl solutions at high temperatures and pressures, *Am. J. Sci., 263*, 445-454.
Teng, H., A. Yamasaki, M.-K. Chun and H. Lee, 1997, Solubility of liquid CO_2 in water at temperatures from 278K to 293K and pressures from 6.44 MPa to 29.49 MPa and densities of the corresponding aqueous solutions, *J. Chem. Thermodynamics, 29*, 1301-1310.
Tödheide, K. and E. U. Franck, 1963, Das Zweiphasengebiet und die kritische Kurve im System Kohlendioxide-Wasser bis zu Drucken von 3500 bar, *Z. Phys. Chemie Neue Folge, 37*, 387-401.
Venyaminov, S. Y. and F. G. Prendergast, 1997, Water (H_2O and D_2O) molar absorptivity in the 1000-4000 cm^{-1} range and quantitative infrared spectroscopy of aqueous solutions, *Anal. Biochem., 248*, 234-245.
Wagner, W., J. R. Cooper, A. Dittmann, J. Kijima, H.-J. Kretzschmar, A. Kruse, R. Mareš, K. Oguchi, H. Sato, I. Stöcker, O. Šifner, Y. Takaishi, I. Tanisjita, J. Trübenbach and T. Willkommen, 2000, Release on the IAPWS industrial formulation 1997 for the thermodynamic properties of water and steam, *J.Eng. Gas Turbines & Power, 122, #1*, 150-184.
Wawersik, W. R., J. W. Rudnicki, P. Dove, J. Harris, J. M. Logan, L. Pyrak-Nolte, F. M. Orr Jr., P. J. Ortoleva, F. Richter, N. R. Warpinski, J. L. Wilson and T.-F. Wong, 2001, Terrestrial sequestration of CO_2: an assessment of research needs, *Advances in Geophysics, 43*, 97-177.
Wendland, M., H. Hasse and G. Maurer, 1999, Experimental pressure-temperature data on three- and four-phase equilibria of fluid, hydrate, and ice phases in the system carbon dioxide-water, *J. Chem. Eng. Data, 44*, 901-906.
Wiebe, R. and V. L. Gaddy, 1939, The solubility in water of carbon dioxide at 50, 75 and 100°C, at pressures to 700 atmospheres, *J. Am. Chem. Soc., 61*, 315-318.
Wiebe, R. and V. L. Gaddy, 1940, The solubility of carbon dioxide in water at various temperatures from 12 to 40° and at pressures to 500 atmospheres: critical phenomena, *J. Am. Chem. Soc., 62*, 815-817.
Xu, T., J. A. Apps and K. Pruess, 2004, Numerical simulation of CO_2 disposal by mineral trapping in deep aquifers, *Appl. Geochem., 19*, 917-936.
Xu, T., J. A. Apps and K. Pruess, 2005, Mineral sequestration of carbon dioxide in a sandstone-shale system, *Chem. Geol., 217*, 295-318.
Yasunishi, A. and F. Yoshida, 1979, Solubility of carbon dioxide in aqueous electrolyte solutions, *J. Chem. Eng. Data, 24, # 1*, 11-14.
Zakirov, I. V., 1984, The P-V-T relations in the H_2O-CO_2 system at 300 and 400°C up to 1000 bar, *Geochem. Int., 6*, 805-811.
Zhang, X. and C. J. Spiers, 2005, Compaction of granular calcite by pressure solution at room temperature and effects of pore fluid chemistry, *Int. J. Rock Mech. Min. Sci., 42*, 950-960.
Zysset, M. and P. W. Schindler, 1996, The proton promoted dissolution kinetics of K-montmorillonite, *Geochim. Cosmochim. Acta, 60, # 6*, 921-931.

Appendix 1 Equations of State for CO_2, H_2O and the CO_2-H_2O system

A. The Equation of State for carbon dioxide

The EOS developed by Duan et al. (1992) is based on the Equation of State of Lee and Kessler (1975) and has the following final form:

$$Z = \frac{PV}{RT} = \frac{P_r V_r}{T_r} = 1 + \frac{B}{V_r} + \frac{C}{V_r^2} + \frac{D}{V_r^4} + \frac{E}{V_r^5} + \frac{F}{V_r^2}\left(\beta + \frac{\gamma}{V_r^2}\right)\exp\left(-\frac{\gamma}{V_r^2}\right) \qquad \text{(A1)}$$

where $B = a_1 + \frac{a_2}{T_r^2} + \frac{a_3}{T_r^3}$ (A2)

$$C = a_4 + \frac{a_5}{T_r^2} + \frac{a_6}{T_r^3} \qquad \text{(A3)}$$

$$D = a_7 + \frac{a_8}{T_r^2} + \frac{a_9}{T_r^3} \qquad \text{(A4)}$$

$$E = a_{10} + \frac{a_{11}}{T_r^2} + \frac{a_{12}}{T_r^3} \qquad \text{(A5)}$$

$$F = \frac{\alpha}{T_r^3} \qquad \text{(A6)}$$

with $P_r = \frac{P}{P_c}$ (A7)

$$T_r = \frac{T}{T_c} \qquad \text{(A8)}$$

$$V_r = \frac{V}{V_c} \qquad \text{(A9)}$$

Table A1 EOS parameters for CO_2 and H_2O

parameter	CO_2	H_2O
a_1	$8.99288497 \cdot 10^{-2}$	$8.64449220 \cdot 10^{-2}$
a_2	$-4.97483127 \cdot 10^{-1}$	$-3.96918955 \cdot 10^{-1}$
a_3	$4.77922245 \cdot 10^{-2}$	$-5.73334886 \cdot 10^{-2}$
a_4	$1.03808883 \cdot 10^{-2}$	$-2.93893000 \cdot 10^{-4}$
a_5	$-2.82516861 \cdot 10^{-2}$	$-4.15775512 \cdot 10^{-3}$
a_6	$9.49887563 \cdot 10^{-2}$	$1.99496791 \cdot 10^{-2}$
a_7	$5.20600880 \cdot 10^{-4}$	$1.18901426 \cdot 10^{-4}$
a_8	$-2.93540971 \cdot 10^{-4}$	$1.55212063 \cdot 10^{-4}$
a_9	$-1.77265112 \cdot 10^{-3}$	$-1.06855859 \cdot 10^{-4}$
a_{10}	$-2.51101973 \cdot 10^{-5}$	$-4.93197697 \cdot 10^{-6}$
a_{11}	$8.93353441 \cdot 10^{-5}$	$-2.73739155 \cdot 10^{-6}$
a_{12}	$7.88998563 \cdot 10^{-5}$	$2.65571238 \cdot 10^{-6}$
α	$-1.66727022 \cdot 10^{-2}$	$8.96079018 \cdot 10^{-3}$
β	1.398	4.02
γ	$2.96 \cdot 10^{-2}$	$2.57 \cdot 10^{-2}$

where V_c is not the critical volume but is defined as follows

$$V_c = \frac{RT_c}{P_c} \qquad \text{(A10)}$$

P_c and T_c are the critical pressure and temperature for CO_2 (Table 2), and P_r and T_r the reduced pressure and temperature, defined as $P_r = P/P_c$ and $T_r = T/T_c$. The values of the EOS parameters for carbon dioxide, a_i, α, β, and γ, are shown in Table A1.

B. Equation of State for water

The IAWPS-97 covers temperatures from 0 to 800°C up to 1000 bars and temperatures from 800 to 2000°C up to 100 bars. The range of validity of IAWPS-97 is divided into 5 regions, as can be seen in Fig. 15, each covered by a so-called basic equation. For readability, the backward equations, as well as the tables containing the coefficients n_i and exponents I_i and J_i, are omitted, and the interested reader is referred to Wagner et al. (2000).

The boundary between region 2 and 3 is expressed as a simple quadratic pressure-temperature relation, the B23-equation

$$\pi = n_1 + n_2\theta + n_3\theta^2 \tag{B1}$$

where $\pi = P/P^*$ and $\theta = T/T^*$ with P^* = 1 MPa and T^* = 1 K. Equation B1 can also be expressed as a function of temperature

$$\theta = n_4 + \left[(\pi - n_5)/n_3\right]^{1/2} \tag{B2}$$

Both equations cover the pressure-temperature range from 350°C at a pressure of 165.292 bars to 590°C at 1000 bars.

A fundamental equation for the specific Gibbs free energy, $g(p,T)$, describes region 1. The dimensionless Gibbs free energy is defined as $\gamma = g/(RT)$, and all thermodynamic properties within the region 1 can be derived from this equation, by using combinations of $\gamma(\pi,\tau)$ and its derivatives, which reads

$$\frac{g(P,T)}{RT} = \gamma(\pi,\tau) = \sum_{i=1}^{34} n_i (7.1-\pi)^{I_i} (\tau - 1.222)^{J_i} \tag{B3}$$

where $\pi = P/P^*$ and $\tau = T/T^*$ with P^* = 16.53 MPa and T^* = 1386K, R = 0.461526 kJ/kg K. This equation is valid for temperatures between 0 and 350°C and pressures from the saturation line up to 1000 bars.

Region 2 is also covered by a fundamental equation for the specific Gibbs free energy. This equation is expressed as $\gamma = g/(RT)$, and is separated in an ideal-gas part γ^0 and a residual part γ^r, as follows

$$\frac{g(P,T)}{RT} = \gamma(\pi,\tau) = \gamma^0(\pi,\tau) + \gamma^r(\pi,\tau) \tag{B4}$$

where $\pi = P/P^*$ and $\tau = T/T^*$ with P^* = 1 MPa and T^* = 540 K, R = 0.461526 kJ/kg K. The ideal-gas part γ^0 is read as

$$\gamma^0 = \ln\pi + \sum_{i=1}^{9} n_i^0 \tau^{J_i^0} \tag{B5}$$

where $\pi = P/P^*$ and $\tau = T/T^*$ with P^* = 1 MPa and T^* = 540 K. The residual part γ^r is given as

$$\gamma^r = \sum_{i=1}^{43} n_i \pi^{I_i} (\tau - 0.5)^{J_i} \tag{B6}$$

where $\pi = P/P^*$ and $\tau = T/T^*$ with P^* = 1 MPa and T^* = 540 K. Equation B4 is valid for temperatures from 0 to 350°C and pressures up to the saturation pressure, for temperatures from 350 to 590°C the upper limit for pressure is described by the B23-equation, and pressure can go up to 1000 bars for temperatures from 590 to 800°C. It should be noted, however, that though the equation yields reasonable values for the single-phase vapour region and the meta-stable vapour region for pressures of more than 100 bars it does not so in the meta-stable vapour region for pressures below 100 bars. A supplementary equation is given to describe this part of the meta-stable vapour region. The form of the dimensionless Gibbs free energy is the same, consisting of an ideal-gas part and a residual part. The

ideal-gas part is identical to Eq. B5 except for the values of the coefficients n_1^0 and n_2^0. The residual part is defined as follows

$$\gamma^r = \sum_{i=1}^{13} n_i \pi^{I_i} (\tau - 0.5)^{J_i} \tag{B7}$$

where $\pi = P/P^*$ and $\tau = T/T^*$ with $P^* = 1$ MPa and $T^* = 540$ K.

The region in between region 1 and 2, region 3, is covered by a fundamental equation for the specific Helmholtz free energy $f(\rho,T)$. The equation of the dimensionless Helmholtz free energy has the form $\varphi = f/RT$, and is expressed as

$$\frac{f(\rho,T)}{RT} = \phi(\delta,\tau) = n_1 \ln\delta + \sum_{i=2}^{40} n_i \delta^{I_i} \tau^{J_i} \tag{B8}$$

where $\delta = \rho/\rho^*$ and $\tau = T/T^*$ with $\rho^* = \rho_c$ and $T^* = T_c$, and $R = 0.461526$ kJ/kg K. Equation B8 describes the thermodynamic properties of water accurately at temperatures from 350 to the boundary between region 2 and 3, and pressures going from the boundary up to 1000 bars. Not only does Eq. B8 give reasonable values for the stable single-phase region but also for the meta-stable regions of superheated liquid and sub-cooled steam.

The saturation curve is coined region 4 and is covered by a saturation-pressure equation $P_s(T)$, which is an implicit quadratic equation. Solving this equation for saturation pressure gives

$$\frac{P_s}{P^*} = \left[\frac{2C}{-B + (B^2 - 4AC)^{1/2}} \right]^4 \tag{B9}$$

where P* = 1 MPa, and

$$A = \upsilon^2 + n_1\upsilon + n_2 \tag{B10a}$$
$$B = n_3\upsilon^2 + n_4\upsilon + n_5 \tag{B10b}$$
$$C = n_6\upsilon^2 + n_7\upsilon + n_8 \tag{B10c}$$

with $\upsilon = \frac{T_s}{T^*} + \frac{n_9}{(T_s/T^*) - n_{10}}$ (B11)

This equation is valid along the entire vapour-liquid saturation line, going from the triple point temperature T_t to the critical temperature T_c and, through extrapolation, covers the temperature range from 0 to 373.946°C.

The high-temperature region 5 also covered by a fundamental equation for the specific Gibbs free energy, which is defined as

$$\frac{g(P,T)}{RT} = \gamma(\pi,\tau) = \gamma^0(\pi,\tau) + \gamma^r(\pi,\tau) \tag{B12}$$

where $\pi = P/P^*$ and $\tau = T/T^*$ with $P^* = 1$ MPa and $T^* = 1000$ K, $R = 0.461526$ kJ/kg K. Equation B12 is divided in an ideal-gas and a residual part, of which the ideal-gas part γ^0 is described as

$$\gamma^0 = \ln\pi + \sum_{i=1}^{6} n_i^0 \tau^{J_i^0} \tag{B13}$$

where $\pi = P/P^*$ and $\tau = T/T^*$ with $P^* = 1$ MPa and $T^* = 1000$ K. And the residual part γ^r is given as

$$\gamma^r = \sum_{i=1}^{5} n_i \pi^{I_i} \tau^{J_i} \tag{B14}$$

where $\pi = P/P^*$ and $\tau = T/T^*$ with $P^* = 1$ MPa and $T^* = 1000$ K. Region 5 is covered from 800 to 2000°C and pressures up to 100 bars.

C. Equation of State for the CO_2-H_2O system

The Equation of State developed by Duan et al. (1992b) to describe PVTX data for the CO_2-H_2O system has a similar form as that for the pure end-members. The EOS for mixtures is an extension of their previous EOS for pure end-members, and pure system behaviour is interpolated to binary and ternary systems by using mixing rules. The pressure-temperature range for applying this Equation of State is from 50 to 1000°C and 0 to 1000 bars. The Equation of State is described as follows

$$Z = 1 + \frac{BV_c}{V} + \frac{CV_c^2}{V^2} + \frac{DV_c^4}{V^4} + \frac{EV_c^5}{V^5} + \frac{FV_c^2}{V^2}\left(\beta + \frac{\gamma V_c^2}{V^2}\right)\exp\left(-\frac{\gamma V_c^2}{V^2}\right) \qquad \text{(C1)}$$

where $V_c = RT_c/P_c$ and B, C, D, E, and F are function of temperature, similar to equations A2 to A6. The EOS for single component behaviour can now be extrapolated to mixed system behaviour by assuming that the parameters in the EOS (e.g. B, C, etc.) at constant temperature and pressure are a function of composition of the mixture. The equations that give this composition dependence of the coefficients are called mixing rules. All equations are given in Table C1, and it should be noted that for binary systems, like the CO_2-H_2O system, there is only one second order B_{ij} parameter and two third order parameters corresponding to $x^2_i x_j$ and $x^2_j x_i$. As we are particularly interested in the binary carbon dioxide-water system only the products BV_c, CV_c^2, FV_c^2, β, and γV_c^2 are important. The third order parameters C_{ijk} and γ_{ijk} can now be expressed as, for example

$$C_{iij} = ((2C_i^{1/3} + C_j^{1/3})/3)^3\, k_{2,iij} \qquad \text{(C2)}$$

where $k_{2,iij}$ is a third order binary parameter, which can be adjusted to give a similar expression for C_{jji} as a function of $k_{2,jji}$. In addition, it is also assumed that

$$k_{2,iij} = k_{2,jji} \qquad \text{(C3)}$$

Table C1 Mixing rules for equations C1 and C5

$BV_c = \sum_i \sum_j x_i x_j B_{ij} C_{c,ij}$ $B' = 2\sum_i x_j B_{ij} V_{c,ij}$	$B_{ij} = ((B_i^{1/3} + B_j^{1/3})/2)^3 k_{1,ij}$ $k_{1,ij} = 1$ (if $i = j$) $V_{c,ij} = ((V_i^{1/3} + V_j^{1/3})/2)^3$
$CV_c^2 = \sum_i \sum_j \sum_k x_i x_j x_k C_{ijk} V_{c,ijk}^2$ $C' = 3\sum_j \sum_k x_j x_k C_{ijk} V_{c,ijk}^2$	$C_{ijk} = ((C_i^{1/3} + C_j^{1/3} + C_k^{1/3})/3)^3\, k_{2,ijk}$ $k_{2,ijk} = 1$ (if $i = j = k$) $V_{c,ijk} = ((V_{c,i}^{1/3} + V_{c,j}^{1/3} + V_{c,k}^{1/3})/3)^3$
$DV_c^4 = \sum_i \sum_j \sum_k \sum_l \sum_m x_i x_j x_k x_l x_m D_{ijklm} V_{c,ijklm}^4$ $D' = 5\sum_j \sum_k \sum_l \sum_m x_j x_k x_l x_m D_{ijklm} V_{c,ijklm}^4$	$D_{ijklm} = (D_i^{1/3} + D_j^{1/3} + D_k^{1/3} + D_l^{1/3} + D_m^{1/3})/5)^3$ $V_{c,ijklm} = ((V_{c,i}^{1/3} + V_{c,j}^{1/3} + V_{c,k}^{1/3} + V_{c,l}^{1/3} + V_{c,m}^{1/3})/3)^3$
$EV_c^5 = \sum_i \sum_j \sum_k \sum_l \sum_m \sum_n x_i x_j x_k x_l x_m x_n E_{ijklmn} V_{c,ijklmn}^5$ $E' = 6\sum_j \sum_k \sum_l \sum_m \sum_n x_j x_k x_l x_m x_n E_{ijklmn} V_{c,ijklmn}^5$	$E_{ijklmn} = ((E_i^{1/3} + E_j^{1/3} + E_k^{1/3} + E_l^{1/3} + E_m^{1/3} + E_n^{1/3})/6)^3$ $V_{c,ij} = ((V_{c,i}^{1/3} + V_{c,j}^{1/3})/2)^3$
$FV_c^2 = \sum_i \sum_j x_i x_j F_{ij} V_{c,ij}^2$ $F' = 2\sum_j x_j F_{ij} V_{c,ij}^2$	$F_{ij} = ((F_i^{1/3} + F_j^{1/3})/2)^3$ $V_{c,ij} = ((V_{c,i}^{1/3} + V_{c,j}^{1/3})/2)^3$
$\beta = \sum_i x_i \beta_i$ $\beta' = \beta_i$	
$\gamma V_c^2 = \sum_i \sum_j \sum_k x_i x_j x_k \gamma_{ijk} V_{c,ijk}^2$ $\gamma' = 3\sum_j \sum_k x_j x_k \gamma_{ijk} V_{c,ijk}^2$	$\gamma_{ijk} = ((\gamma_i^{1/3} + \gamma_j^{1/3} + \gamma_k^{1/3})/3)^3\, k_{3,ijk}$ $k_{3,ijk} = 1$ (if $i = j = k$) $V_{c,ijk} = ((V_{c,i}^{1/3} + V_{c,j}^{1/3} + V_{c,k}^{1/3})/3)^3$

The same assumption is made for k_3 and the binary interaction parameters for the system CO_2-H_2O system, as a function of temperature, are described in Table C2.

One application of the EOS for mixtures is to calculate phase equilibria, for which the partial fugacity coefficients are needed. Partial fugacity, partial fugacity coefficient and chemical potential are describes as

$$\mu_i(T,P,X) = \mu_i^o(T) + RT\ln f_i(T,P,X) \quad \text{, or}$$
$$\mu_i(T,P,X) = \mu_i^o(T) + RT\ln \varphi_i(T,P,X)x_i P \qquad \text{(C4)}$$

where μ_i is the chemical potential of species i, μ_i^o is the standard chemical potential, e.g. the chemical potential at 1 bar fugacity, f_i is the partial fugacity of species i, φ_i the partial fugacity coefficient of species i, x_i the mole fraction of species i in the mixture, and P the pressure. The partial fugacity coefficients of species in the mixture can be calculated with

$$\ln\varphi_i = -\ln(Z) + \frac{B'}{V} + \frac{C'}{2V^2} + \frac{D'}{4V^4} + \frac{E'}{5V^5} + \frac{F'\beta + \beta' FV_c^2}{2\gamma V_c^2}\left(1 - \exp\left(-\frac{\gamma V_c^2}{V^2}\right)\right)$$
$$+ \frac{F'\gamma V_c^2 + \gamma' FV_c^2 - FV_c^2\beta\left(\gamma' - \gamma V_c^2\right)}{2\left(\gamma V_c^2\right)^2} \times \left(1 - \left(\frac{\gamma V_c^2}{V^2} + 1\right)\exp\left(-\frac{\gamma V_c^2}{V^2}\right)\right) - \frac{\left(\gamma' - \gamma V_c^2\right)FV_c^2}{2\left(\gamma V_c\right)^2} \qquad \text{(C5)}$$
$$\times\left(2 - \left(\frac{\left(\gamma V_c^2\right)^2}{V^4} + \frac{2\gamma V_c^2}{V^2} + 2\right)\exp\left(-\frac{\gamma V_c^2}{V^2}\right)\right)$$

where B', C', D', E', F', β', and γ' are derivatives (Table C1). The other components are the same as in previous equations (Tables A1 and C1).

The Equation of State described above can very well predict the effect of non-ideal mixing. The excess volume is a property that can represent this behaviour

$$V_{ex} = V^M - \sum x_i V_i^{pure} \qquad \text{(C6)}$$

where V^M is the molar volume of the mixture and V_i^{pure} the molar volume of the separate pure species, multiplied by their molar fractions in the mixture, x_i.

Table C2 Binary interaction parameters, as a function of T(K), for the CO_2-H_2O system	
50 –100°C	k_1 = 0.20611 + 0.0006T k_2 = 0.8023278 – 0.0022206T + 184.76824/T k_3 = 1.80544 – 0.0032605T
100 - 222°C	k_1 = -10084.5042 – 4.27134485T + 256477.783/T + 0.00166997474T^2 k_2 = 9.000263 – 0.00623494T –2307.7125/T k_3 = -74.1163 + 0.1800496T –1.40904946·10^{-4}T^2 + 10130.5246/T
222 - 350°C	k_1 = -0.3568 + 7.8888·10^{-4}T + 333.399/T k_2 = -19.97444 + 0.0192515T + 5707.4229/T k_3 =12.1308 – 0.0099489T – 3042.09583/T
350 - 1000°C	k_1 = -4.53122 + 0.0042113T + 1619.7/T k_2 =-163.4855 + 0.190552T –7.228514·10^{-5}T^2 + 46082.885/T k_3 = 1.7137 – 6.7136·10^{-4}T